Journal of Scientific & Industrial Research
Vol. 84, June 2025, pp. 627-644
DOI: 10.56042/jsir.v84i6.12636

A Single–Degree–of–Freedom Solution Procedure to Determine Dynamic Characteristics of Air–Bearing

Muruganandam Muthanandam

Department of Mechanical Engineering, PSN College of Engineering and Technology, Tirunelveli 627 152, Tamil Nadu, India

Received 22 July 2024; revised 19 March 2025; accepted 22 May 2025

An externally–pressurized journal air–bearing for a heavy, rigid, and balanced rotor is analyzed. The dynamic characteristics of air–bearing are determined during the investigation, at various angular velocities of the journal and angular frequencies of journal vibration. The dynamic characteristics of the air–bearing are found by a numerical simulation procedure. The journal air–bearing system is modeled to have a single–degree–of–freedom. The journal follows a predefined harmonic motion during the simulation. This motion is caused by self–exciting forces resulting from flow dynamics within a real air–bearing. Pressure distribution in the air–bearing is computed by solving the two–dimensional Reynolds equation. Alternating–direction finite–difference method is implemented using MATLAB to find the numerical solutions for pressure. The dynamic load–carrying capacity is calculated via the numerical integration of pressure distribution. The dynamic characteristics of air–bearing are calculated using the time series of displacements, velocities of the geometric center of the journal, and air–bearing forces. The stiffness coefficients and damping coefficients of air–bearing, as well as the eccentricity ratio and attitude angle of the journal, are compared with the findings in the literature. The average percentage differences in the results are attributed to the minor differences in the mathematical models of air–bearing used in this research and the literature. The dynamic stability of the rotor air–bearing system against self–excited vibration can be examined using the dynamic characteristics of the air–bearing.

Keywords: Dynamic coefficients, Gas–lubricated, Hydrostatic journal bearing, Numerical simulation, Self–excited vibration

Introduction

Air bearings find applications in grinding wheels, micro gas turbines, dental drills, textile mill spindles, etc. When compared with oil, air has a smaller viscosity. Hence, air bearings are useful in lighter–weight machines that rotate at higher speeds. Oil bearings are not suitable for such high–speed applications. Air bearings are subjected to a kind of dynamic instability known as Self–Excited (SE) vibration[1] to a greater extent than oil bearings due to their smaller damping coefficient. A significant barrier to the broad real–world applications of air bearings in high–speed machinery is the phenomenon of SE vibration. Lund[2] concluded that the threshold speed of SE vibration could be greatly raised, much over the rotor's threshold speed in rigidly supported bearings, if the bearing support had a damping characteristic in addition to flexibility. The frequency of instability decreases simultaneously with the rise of the threshold speed. Powell & Tempest[3] demonstrated the application of rubber O–rings for the SE whirl stabilization of high–speed machines. Except for Viton—Fluorinated hydrocarbon, the effectiveness of each type of rubber tested in suppressing the SE whirl decreased with temperature. The air film stiffness is increased by either raising the bearing supply pressure (p_s) for a given bearing clearance or reducing the bearing clearance for a given bearing p_s. Greater air film stiffness enhances rubber's ability to absorb energy and prevents SE vibration. Majumdar[4] made a theoretical analysis of the stability of an externally–pressurized air journal bearing with O–ring–supported bushings. This analysis showed that the dynamic stability of air bearings could be improved by increasing the aerostatic stiffness. The analytical results of Majumdar[4], which showed that the ability of the rubber O–ring to limit the SE vibration is derived from its ability to absorb energy from the air film, were in good agreement with the experimental findings by Powell & Tempest.[3] Majumdar[4] emphasized that the dynamic properties of the rubber O–ring and aerostatic stiffness needed attention for effective absorption of SE vibrational energy by the rubber O–ring. Belforte *et al.*[5] presented the details of a test rig used to experiment with the development of

Author for Correspondence
E-mail: m.muruganandam@psncet.ac.in

air bearings. The results of the experimentation on the stability analysis of externally−pressurized Air–Bearing (AB) floating on O–rings were presented in the form of records of rotor orbits at two radial bushings, displacement signal frequency spectrum, and displacement amplitude at different speeds. These results showed that the rotor was stable and did not present whirl instability. The studies[2–5] explained that SE vibration could be avoided by introducing an elastic supporting structure in the form of O–rings between the bearing bushing and the casing, characterized by properly selected dynamic characteristics or Dynamic Coefficients (DC) such as stiffness and damping coefficients.

Brzeski & Kazimierski[6] explained a theoretical model to compute the pressure(p) distribution in an externally–pressurized air–bearing with an Air–Ring (AR) or Air–Ring Bearing (ARB) and its Load–Carrying Capacity (LCC). In an ARB, there are two circular layers of air: an inner layer (AB) between the journal and the bushing and an outer layer (AR) between the bushing and the casing. A preliminary investigation of ARB was made to determine: mass flow rate of air through Feed–Hole (FH), LCC, and displacement of Geometric Center of the journal (CG_J), both theoretically and experimentally, at various p_s. Both these results indicated that ARB was a high–stiffness bearing. The stable motion of the rotor was verified during the investigation. Czołczyński[7] presented the equations of free–vibrations of the Rotor Air–Ring Bearing System (RARBS) in cylindrical and conical modes. The dynamic stability of the RARBS was verified by solving these equations. Theoretical results of the bearing characteristics, such as LCC and the power consumption per unit load for various dimensions of the following two types of geometry of FH in ARB: plain FH and pocketed FH, were verified using experimental results.[8] It was found that these bearing characteristics depended on the FH geometry. During the analysis of the dynamic response of ARB to a step–change in force, the p distributions in AB and AR regions of ARB were computed by solving Reynolds Equation (RE).[9] The dynamic components of LCC of ARB were calculated by integrating the instantaneous p distribution. Equations of motion of the journal and the bushing were employed to predict the displacement of CG_J and the geometric center of the bushing (CG_B) with respect to time. Numerical simulations were performed to determine the DC of externally–pressurized journal air bearings.[10] During the simulations, the CG_J follows a Simple Harmonic Motion (SHM). Dynamic components of LCC were written as linear combinations of displacements and velocities of CG_J. Both the linear and nonlinear DC of AB were presented as functions of angular velocities (ω) of the journal and angular frequencies (v) of the journal vibration. Identical RE were used for calculating p–distribution in AR and AB regions of ARB to estimate its DC.[11] The effects of various parameters of ARB, such as AR clearance (c_{AR}), number of rubber baffles, FH orifice diameter (d_o), FH chamber diameter (d_c), and FH chamber depth (h_c) on the DC of AR were studied. The linear DC of AR were presented as functions of v. In comparison to a direct FH geometry, a chamber FH geometry of ARB provided stability to the RARBS under SE whirl conditions.[12] The analysis of an AB system for a turbine rotor having symmetrical loading was carried out by mathematical modeling and numerical simulation of CG_J motion.[13,14] The stability threshold speed was estimated from the linearized equations of motion using the techniques of Czołczyński.[7]

O–rings made of solid elastomeric material were used as bushing supports to inhibit SE vibration in air bearings.[2–5] An elastic supporting structure could be realized in practice via an externally–pressurized AR.[1,6–18] A Single–Degree–Of–Freedom (1–DOF) solution procedure was employed previously in studies[6–14] that investigated SE vibration in ARB. A Two–Degrees–Of–Freedom (2–DOF) approach to ARB analysis was made in the literature.[1,15–17]

When compared to the 2–DOF approach[1,15–17], the limitations of the 1–DOF approach[6–14] are outlined as follows:

1. In the 1–DOF approach, p distributions in the AB and AR regions were analyzed by solving RE independently in each region. This approach resulted in the independent determination of DC in each region. The simultaneous computations of the p distribution in AB and AR regions were made by solving the full Three–Dimensional (3–D) equations of fluid motion in the 2–DOF approach. Hence, the DC of both AB and AR were determined simultaneously by considering the interaction between the AR and the AB regions through the FH in the bushing.
2. It is shown in this paper that the term in the RE that represents the mass flow rate per unit volume due to the velocity–induced flow would not be present to compute the p–distribution in the AR region, as the bushing does not rotate. But the

identical RE were used for calculating *p*–distribution in AR and AB regions in the 1–DOF solution procedure. In the 2–DOF approach, the differential equations of motion of air, through the FH passages, AR, and AB regions, were solved via a 3–D Computational Fluid Dynamics (CFD) approach. The 3–D geometry of the airflow domain in the ARB was generated. The ARB geometry was exported for computational grid generation. The fluid flow domain was discretized into hexahedral finite control volumes (cells). Individual boundary faces of the flow domain were identified to specify the following operating conditions: the journal undergoes rotation during Steady–State Simulation (SSS); the journal rotates as well as translates, and the bushing translates during Transient–State Simulation (TSS). See the literature[15,16] for more details.

3. To determine the DC of AB in 1–DOF solution procedure, the CG_B was fixed, and the CG_J was displaced to follow an SHM. Similarly, CG_B was prescribed to follow an SHM to find the DC of AR by fixing the position of CG_J. Due to the aforementioned reason, this study is named the 1–DOF solution procedure in this paper. At each time–step of SHM of the journal in the 2–DOF approach, corresponding to a prescribed eccentric position of CG_J with respect to the Static Equilibrium Position (SEP), *p*–distributions in both AB and AR regions were computed. The instantaneous spatial distribution of *p* around the bushing (in both the AB and AR regions) eventually governed the instantaneous position of CG_B. The *p*-distribution so computed also governed the mass flow rates of air into the AB for a specified p_s at the inlet to AR. An integration of *p*-distribution over the journal and the bushing surfaces gave the instantaneous LCC of the ARB. Timeseries of displacement, velocity, and LCC were used to evaluate the DC of AR and AB in a coupled manner. Thus, the DC of both AB and AR were determined simultaneously. Since the motions of both CG_J and CG_B are coupled together during numerical simulation, this procedure is referred to in this paper as a 2–DOF approach.
4. In 1–DOF solution procedure, zero–dimensional (algebraic) equations were used to calculate the air mass flow through FH into the AR and AB regions. The FH restrictor's dimensions were disregarded, and instead, the FH was treated as a point source. The empirical discharge coefficient was used to calculate the mass flow rate. Significant calculation errors may result from such a simplistic model of the orifice, according to reports.[18] In 2–DOF approach, differential equations of motion of air through the FH passages were solved via a 3–D CFD technique. The instantaneous spatial distributions of *p* at both the AB and the AR regions of ARB were used to compute the time series of the mass flow rate of air into the AB for a specified p_s at the inlet to ARB and atmospheric *p* at the exit from ARB. The calculation of the orifice's coefficient of discharge is not required since the 3–D CFD technique, which is a virtual test bench, precisely computes the mass flow rates of air by solving differential equations of air motion.
5. For determining the DC in 1–DOF solution procedure, identical p_s were used at inlets to the AB and AR, whereas it is to be expected that there would be a significant pressure loss during air flow through the FH and AR passages. In turn, these *p* at inlet and exit of the FH would determine the mass flow rate of air into the AR and AB as demonstrated by 2–DOF approach.

The main emphasis of the research reported in literature[1,15–17] was a 2–DOF approach for determining the DC of ARB. Since no experimental data was available in the public domain for ARB[18], the DC computed using the 2–DOF approach[1,15–17] could not be validated. An alternate strategy of comparing the results of the 2–DOF approach[1,15–17] with the results of the 1–DOF approach[7] was followed. In the comparison process, it was necessary to carry out simulations on the AB part of ARB using the 1–DOF approach. Also, the mathematical model and the computing procedure of AB in the 1–DOF approach were not explained in detail in the literature.[7] It was needed to refer to other literature during simulations on AB using the 1–DOF approach. The need for literature that explained the mathematical model of AB and demonstrated the entire computing procedure using the 1–DOF approach was strongly felt. *Thus, the presentation in this paper is an outcome of a part of the strategy to validate the results of dynamic characteristics of air–ring bearings determined by the 2–DOF approach.*[1,15–17]

In this paper, the mathematical model of AB is explained and a procedure to compute the DC of AB

(Figs 1 and 2) at various ω and v is demonstrated. In Fig. 1, the DC, $K_{AB}^{(ij)}$ and $C_{AB}^{(ij)}$ represent the stiffness coefficient and the damping coefficient, respectively. The superscripts i and j in $K_{AB}^{(ij)}$ and $C_{AB}^{(ij)}$ are used to indicate the bearing forces on the journal in direction i when CG_J moves along direction j (i and j can be x or y). The computation of these coefficients is done by solving a Two–Dimensional (2–D) RE. The dimensions and operating conditions of AB are: mass of rotor m_R = 228 kg, diameter of journal D_J = 110 mm, length of journal L = 110 mm, radial clearance of AB c_{AB} = 30 μm, number of rows of FH r = 2, number of FH per row n = 8, d_o = 0.3 mm, h_c = 2.5 mm, d_c = 2 mm, maximum rotation speed of rotor S_{max} = 63251 RPM, and p_s = 7 bar. The analysis is made using the mathematical model proposed in the literature.[6] Since the AB is a finite–length bearing having a length–to–diameter (L/D_J) ratio equal to unity, variations in p in both circumferential (θ) and axial directions (z) are significant. Hence, the RE is solved to compute $p(\theta, z)$. Since it would be extremely difficult to obtain analytical solutions for $p(\theta, z)$ by solving this 2–D governing equation, a finite–difference method is implemented using MATLAB to find the numerical solutions for $p(\theta, z)$. p is computed by following the 1–DOF solution procedure given in the literature.[7] The dynamic LCC is found via numerical integration of $p(\theta, z)$. The time series of displacements of the CG_J, velocities of CG_J, and dynamic components of LCC are used to evaluate the DC of AB. The results given in the literature[7]are used as the benchmark to compare the mathematical model of AB used in this paper.

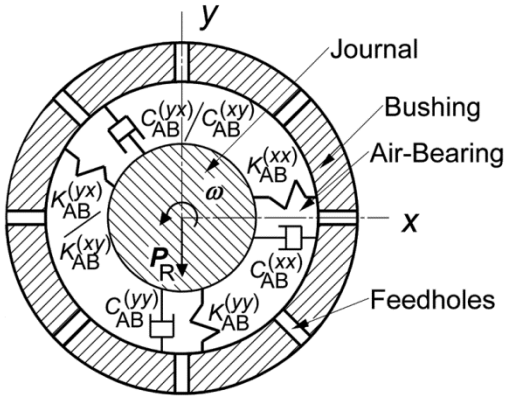

Fig. 1 — Air–bearing (AB) ($K_{AB}^{(ij)}$–Stiffness coefficient, $C_{AB}^{(ij)}$–Damping coefficient, due to the bearing forces on journal in direction i when CG_J moves along direction j; i and j can be x or y; ω–Angular velocity of journal, and P_R–Load on journal AB)

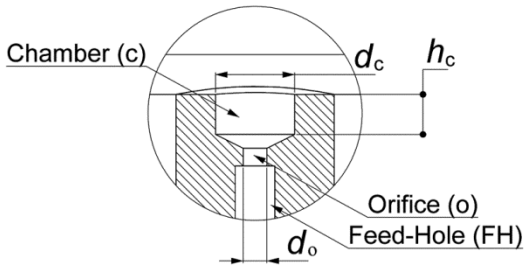

Fig. 2 — Feed–hole (d_c–Chamber diameter, h_c–Chamber height, and d_o–Orifice diameter)

State–Of–The–Art of Journal Air Bearings Design and Analysis

Several new types of aerostatic journal bearings, including the Sixsmith, dual gas film or air–ring bearing, and bushing with tangential orifices, are being investigated as various options to elastomeric support for the bushing in air bearings.[18] The disadvantage of conventional rigidly mounted air bearings is their lower damping coefficients. To overcome this drawback, a new design of air–ring bearings[19] is being investigated. This new air–ring bearing design has an annular region (air–ring) between the movable bushing and the casing. The bushing may be connected to the casing via an elastomer or a beam, bump, or wing–foil design. This setup increases the damping characteristics of the AB system. Numerical analysis of foil bearing designs is made simpler by this air–ring design. Zeise & Schweizer[20] investigated the effect of ring tilting on the dynamic stability against SE vibration of the ARB. Zeise & Schweizer[21] employed RE to compute the p distribution in the ARB with a three–lobe bore geometry design by Finite–Element Method (FEM). Numerical simulations were made to investigate the SE vibration and the bifurcation behavior of the RARBS by mounting the bushing in the casing using a foil structure and an elastomer.

Battig & Schiffmann[22] studied the dynamic instability in the tilting motion of herringbone grooved journal AB bushings experimentally, where the bushings were mounted using flexible supports in the casing. It was verified experimentally that the onset speed of tilting instability was significantly increased by the damping characteristic of the flexible support. Deb *et al*.[23] analyzed the dynamic stability of aerostatic bearings with a finite nozzle diameter to bearing radius ratio. Numerical analysis was carried out to compute the bearing p distribution by solving the RE using a finite volume method. Lu *et al*.[24] analyzed the interaction between the DC of AB and

the thermodynamic properties of rotor AB system. To improve the accuracy of the dynamic and thermal characteristics models of high–speed spindles supported by aerostatic bearings, a thermal–vibration coupling model was proposed.

Wang *et al*.[25], Chen *et al*.[26], and An *et al*.[27] reported a Fluid–Structure Interaction (FSI) procedure to determine the DC of rigidly mounted air bearings. Chen *et al*.[26] employed the 2–D RE, while Wang *et al*.[25] used the 3–D differential equations of motion of air, as the fluid model in the FSI procedure. Chen *et al*.[26] used Galerkin FEM and the Newton–Raphson method to solve the RE, whereas Wang *et al*.[25] used the CFD method to solve the fluid model, for computing the p distribution in the AB. In the structural model of the investigation by Wang *et al*.[25], the rotor was characterized using inertia, spring, and damper elements; however, in the analysis by Chen *et al*.[26], the rotor was characterized as a flexible Timoshenko beam. Chen *et al*.[26] used the transfer matrix method to solve the equation of motion of rotor in order to determine the position of the CG_J, whereas Wang *et al*.[25] used FEM in their study. In both investigations, the DC of AB were calculated using the time series of displacement of CG_J, velocity of CG_J, and LCC of AB when the p distribution and CG_J position data were transferred between the fluid and the structural models at each time–step during the simulation. Both Wang *et al*.[25] and An *et al*.[27] investigated the effects of rotor speed, S and mass of rotor, m_R on the dynamic stability of the rotor AB system using shaft orbits, phase portraits, and frequency response curve. Chen *et al*.[26] examined the influence of rotor manufacturing errors, including roundness, convexity, concavity, and tapers, on the dynamic stability of AB system.

The research in literature[1,15–17] focuses on flexibly mounted air bearings, the ARB, while studies[25–27] deal with rigidly mounted air bearings. The journal is the only moving component in a rigidly mounted AB, while in an ARB, both the journal and bushing are moving components. The journal has radial translation in addition to rotation, and the bushing experiences radial translation in an ARB. The study[1,15,17] has not attempted the combined fluid–structural dynamic analysis. It is possible to use the 3–D CFD simulation methodology with 2–DOF approach[15] as a virtual test bench to predict the dynamic stability of a real ARB by extending it to examine the rotor's orbital motion for a certain set of self–exciting forces.

Materials and Methods

Dynamic Load–Carrying Capacity of Air–Bearing

Mechanical Equilibrium Conditions in a Loaded Air–Bearing

A journal AB that carries a load P_R is shown in Fig. 3. P_R acts vertically downwards through the center O_J. The journal is of length L. At an angular position θ from the attitude line, the film thickness

$$h_{AB} = c_{AB} + e_J^0 \cos\theta \quad \ldots (1)$$

where, c_{AB} is radial clearance; and e_J^0, eccentricity. From the conditions of equilibrium along the attitude line,

$$-F_J^{(R)}(0) + P_R \cos\alpha_J^0 = 0 \quad \ldots (2)$$

where, $F_J^{(R)}(0)$ is radial component of static LCC (force component along the line of centers, see Fig. 3); and α_J^0, attitude angle. In terms of p and shear stress (τ) distributions,

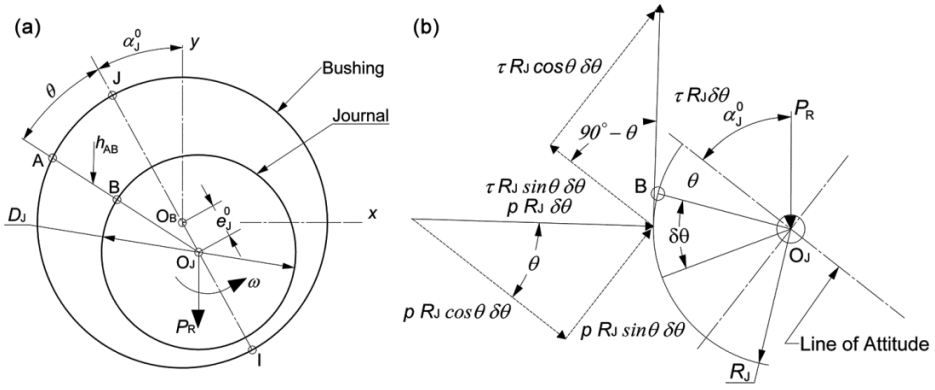

Fig. 3 — (a) A loaded journal bearing at static equilibrium conditions (IJ–Attitude line, e_J^0–Eccentricity, and α_J^0–Attitude angle), (b) Forces on an elemental journal surface (p–Pressure and τ–Shear stress)

$$\int_0^{2\pi}(p\cos\theta)LR_{\mathrm{J}}d\theta-\int_0^{2\pi}(\tau\sin\theta)LR_{\mathrm{J}}d\theta+P_{\mathrm{R}}\cos\alpha_{\mathrm{J}}^0=0 \quad \ldots(3)$$

From conditions of equilibrium in the direction normal to the attitude line (see Fig. 3),

$$F_{\mathrm{J}}^{(T)}(0)-P_{\mathrm{R}}\sin\alpha_{\mathrm{J}}^0=0 \quad \ldots(4)$$

where, $F_{\mathrm{J}}^{(T)}(0)$is tangential component of static LCC. In terms of p and τ distributions,

$$\int_0^{2\pi}(p\sin\theta)LR_{\mathrm{J}}d\theta+\int_0^{2\pi}(\tau\cos\theta)LR_{\mathrm{J}}d\theta-P_{\mathrm{R}}\sin\alpha_{\mathrm{J}}^0=0 \quad \ldots(5)$$

Governing Equation for Pressure Distribution in Air–Bearing

A Control Volume (CV) of finite size fixed in space is considered to carry out the analysis on an AB. This CV has dimensions $R_{\mathrm{J}}d\theta$, h_{AB}, and dz along θ, δ, and z coordinate directions, respectively (see Fig. 4). The RE (6) governs the flow through AB. Analysis of RE is given in Appendix.

$$\frac{\partial(ph_{\mathrm{AB}})}{\partial t}-\frac{\partial}{R_{\mathrm{J}}\partial\theta}\left(\frac{ph_{\mathrm{AB}}^3}{12\mu R_{\mathrm{J}}}\frac{\partial p}{\partial\theta}\right)+\frac{R_{\mathrm{J}}\omega}{2}\frac{\partial(ph_{\mathrm{AB}})}{R_{\mathrm{J}}\partial\theta}-\frac{\partial}{\partial z}\left(\frac{ph_{\mathrm{AB}}^3}{12\mu}\frac{\partial p}{\partial z}\right)=\frac{\mathrm{R}Td\dot{m}_{\mathrm{FH}}}{R_{\mathrm{J}}d\theta dz} \quad \ldots(6)$$

Equation (6) can be written in dimensionless form by defining the non–dimensional variables: $\tau = vt$; $\xi = z/R_{\mathrm{J}}$; $H = h_{\mathrm{AB}}/c_{\mathrm{AB}}$; and $P = p/p_{\mathrm{a}}$, where p_{a} is atmospheric pressure. The RE is written in dimensionless form as

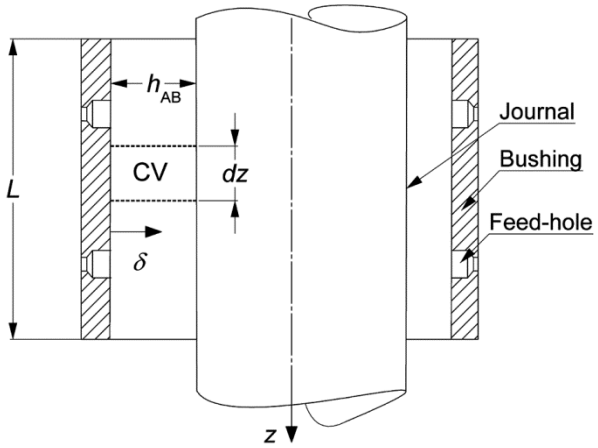

Fig. 4 — Control volume (CV) for the fluid flow through the air–bearing (h_{AB}–Air–bearing film thickness, L–Bearing length, and δ–Radial coordinate)

$$\lambda\frac{\partial(PH)}{\partial\tau}-\frac{\partial}{\partial\theta}\left(PH^3\frac{\partial P}{\partial\theta}\right)+\Lambda\frac{\partial(PH)}{\partial\theta}-\frac{\partial}{\partial\xi}\left(PH^3\frac{\partial P}{\partial\xi}\right)=\frac{d\dot{m}_{\mathrm{FH}}}{\mathrm{C}_1 d\theta d\xi} \quad \ldots(7)$$

where, $\mathrm{C}_1 = p_a^2c_{\mathrm{AB}}^3/(12\mu\mathrm{R}T)$;
$\lambda = 12\mu\nu R_{\mathrm{J}}^2/(p_a c_{\mathrm{AB}}^2)$; $\Lambda = 6\mu\omega R_{\mathrm{J}}^2/(p_a c_{\mathrm{AB}}^2)$;
λ, frequency number; and Λ, speed number.[29]
Substituting $P^2 = Q$ in Eq. (7) and rearranging,

$$\lambda\frac{H}{P}\frac{\partial Q}{\partial\tau}+2\lambda\frac{Q}{P}\frac{\partial H}{\partial\tau}-H^3\left(\frac{\partial^2Q}{\partial\theta^2}+\frac{\partial^2Q}{\partial\xi^2}\right)-3H^2\left[\left(\frac{\partial H}{\partial\theta}\right)\left(\frac{\partial Q}{\partial\theta}\right)+\left(\frac{\partial H}{\partial\xi}\right)\left(\frac{\partial Q}{\partial\xi}\right)\right]+\Lambda\frac{H}{P}\frac{\partial Q}{\partial\theta}+2\Lambda\frac{Q}{P}\frac{\partial H}{\partial\theta}=2\frac{d\dot{m}_{\mathrm{FH}}}{\mathrm{C}_1 d\theta d\xi} \quad \ldots(8)$$

Computation of p distribution in the AB is carried out by solving Eq. (8). The flow domain of the AB is discretized into a set of $M\times N$ grid points where $\Delta\xi = L/(R_{\mathrm{J}}M)$ and $\Delta\theta = 2\pi/N$, as shown in Fig. 5. The discrete p values are determined at the grid points. In Eq. (8), $Q = f(\xi, \theta, \tau)$. Equation (8) consists of two independent spatial variables ξ and θ, in addition to the marching time variable τ. i, j, and n are indices that are used to represent the discrete values of ξ, θ, and τ, respectively. Equation (8) is used to carry out TSS of AB in a 1–DOF approach. In order to carry out SSS of AB in a 1–DOF approach, the transient terms in Eq. (8) are excluded.

As discussed in Introduction Section, the procedure adopted in literature[7] is followed in this paper to carry out the 1–DOF analysis. In this analysis, the bushing is fixed, and the journal is allowed to follow an SHM to determine the DC of AB.

The dimensionless air film thickness H in Eq. (8) is derived from Eq. (1) as

$$H = 1+\epsilon_{\mathrm{J}}^0\cos\theta \quad \ldots(9)$$

Governing Equations for Mass Flow Through the Feed–Holes of Air–Bearing

Air at p_{s} enters the FH chamber (c) through an orifice (o) as shown in Fig. 6. It then flows through an annular orifice (ao) at the mouth of c into the AB and is exhausted to the atmosphere through the bearing ends.

Equations (10) and (11) are arrived at (refer Appendix) that govern the mass flow through FH.

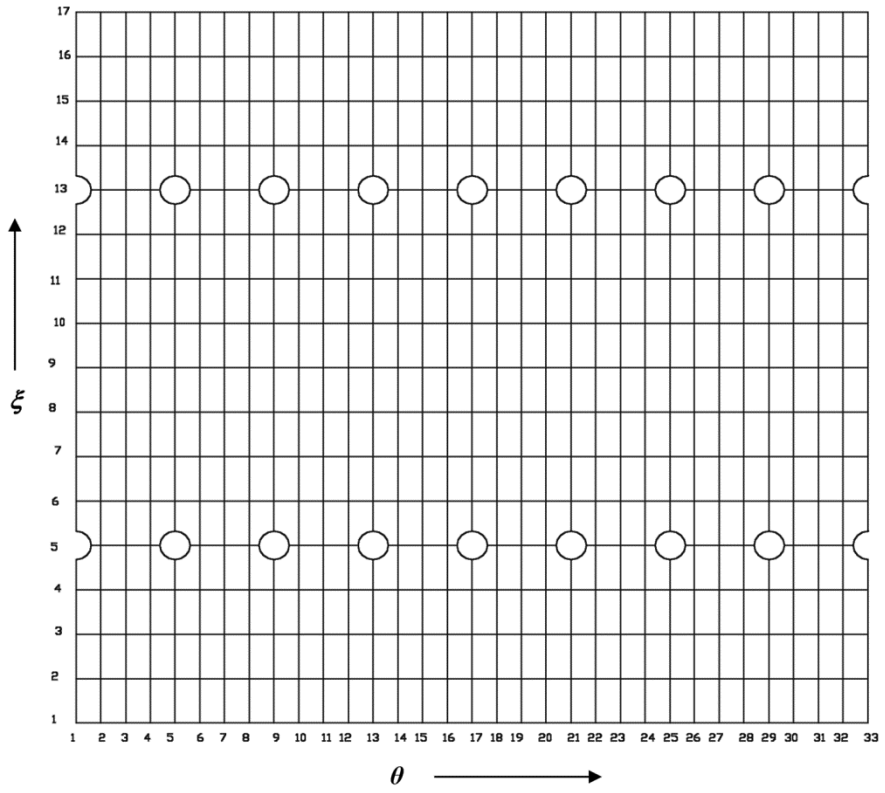

Fig. 5 — Computational grid ($M = 16$, $N = 32$) for pressure distribution ($\Delta\xi = L/(R_J M)$ for $1 \le i \le M + 1$, $\Delta\theta = 2\pi/N$ for $1 \le j \le N + 1$)

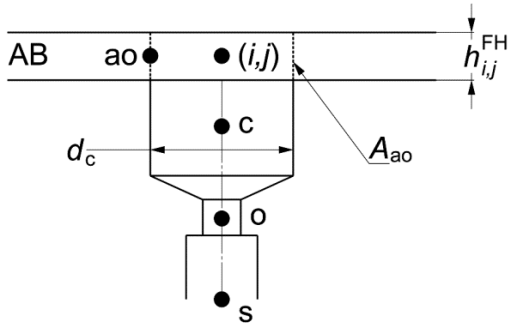

Fig. 6 — Air–bearing (AB) feed–hole (FH) (s–Supply, o–Orifice, c–Chamber, ao–Annular orifice, and A_{ao}–Area of annular orifice)

These equations form two non–linear algebraic equations with two unknowns υ_{FH} and π_{FH}.

$$\left[1 - C_{FH}(1-\beta)\left(1 - \sqrt{1 - \upsilon_{FH}^2}\right)\right]^2 (\pi_{FH}\pi_s)^2 = \frac{1}{2\left[C_2 + \frac{1}{C_2}\right]}\left[\left(Q_{i+1,j}^{FH} + Q_{i-1,j}^{FH}\right)C_2 + \frac{\left(Q_{i,j+1}^{FH} + Q_{i,j-1}^{FH}\right)}{C_2} + \frac{C_3 \upsilon_{FH}\pi_{FH}}{C_1\left(H_{i,j}^{FH}\right)^2}\right] \quad \ldots (10)$$

$$\lim_{\Delta t \to 0} \frac{\pi_{FH} - \pi_{FH,0}}{\Delta t/2}\frac{V_c}{RT} = (C_o \upsilon_o A_o - \upsilon_{FH}\pi_{FH}A_{ao})C_4 \quad \ldots (11)$$

These equations are solved using the Newton–Raphson method to find υ_{FH} and π_{FH}. This solution method is demonstrated in Appendix. Equation (11) is used to carry out TSS of AB in a 1–DOF approach. To carry out SSS of AB in a 1–DOF approach, the transient term on the LHS of Eq. (11) is excluded. The procedure to compute $\dot{m}_{FH}$ is as follows: (i) The constants C_1, C_2, C_3, C_4, A_o, V_c, π_s, and β in Eqs (10) and (11) are calculated for air using (a) the parameters of AB and (b) Fig. 5. (ii) The variables A_{ao} and $H_{i,j}^{FH}$ are found using (a) the parameters of AB and Eq. (9); (iii) Δt is computed using ν; (iv) $Q_{i-1,j}^{FH}$, $Q_{i+1,j}^{FH}$, $Q_{i,j-1}^{FH}$, and $Q_{i,j+1}^{FH}$ are known from the initial condition for the first time–step and known from the previous computations for the forthcoming time–steps; (v) $C_{FH} = f(Re)$ and $Re = f(\upsilon_{FH}, \pi_{FH})$ as seen from Eq. (B13). $C_o = f(\pi_{FH})$, and $\upsilon_o = f(\pi_{FH})$ as seen from Eq. (B16). C_{FH}, C_o, υ_o, υ_{FH} and π_{FH} are solved using the Newton–Raphson method; (vi) $\dot{m}_{FH}$ is computed from Eq. (B5) using υ_{FH} and π_{FH}.

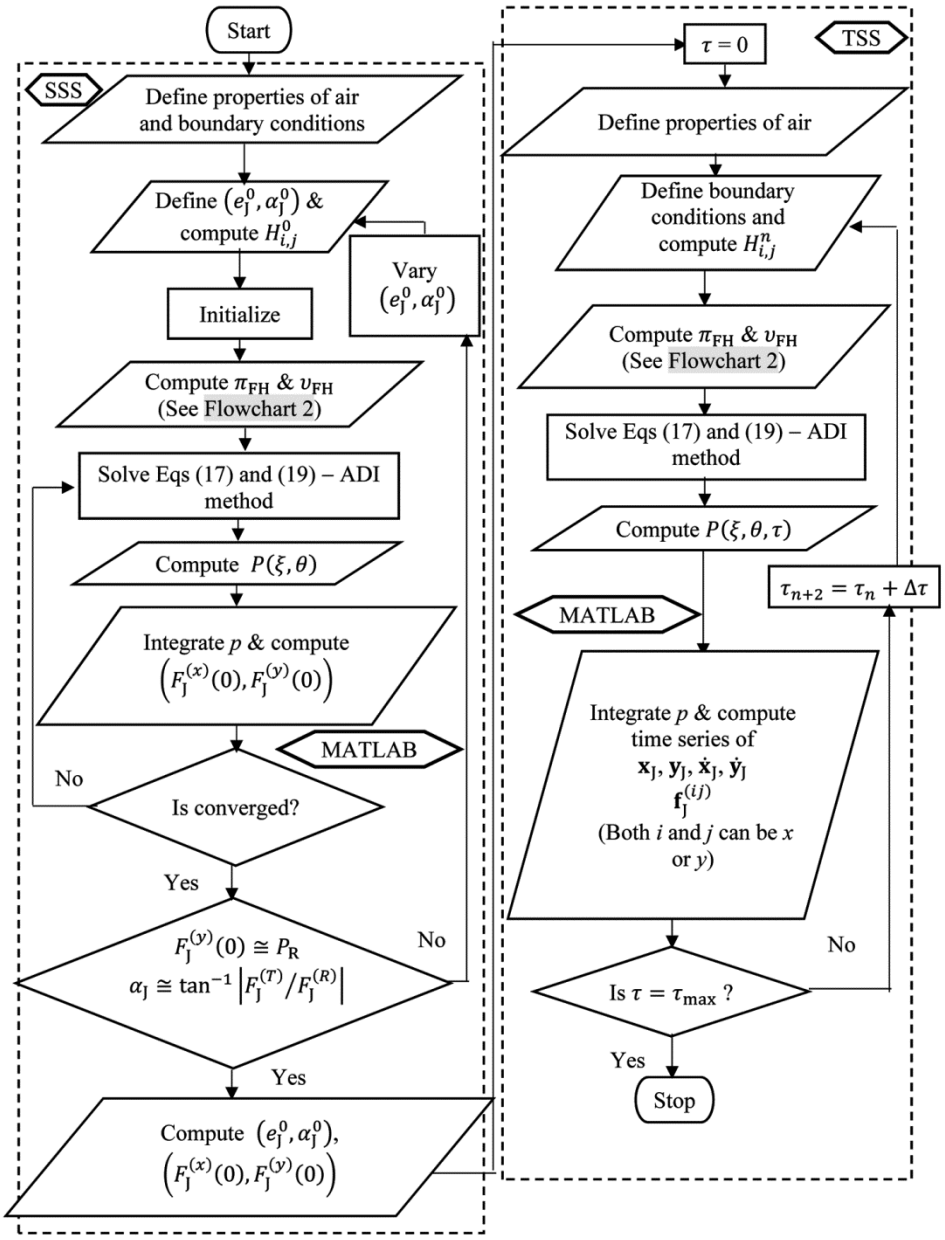

Flowchart 1 — Alternating–direction implicit method of computing load–carrying capacity of air–bearing

Computational Procedure for Load–Carrying Capacity of Air–Bearing

The p distribution fulfills the following two boundary conditions: (i) in ξ–direction, at both ends of the bushing, $p = p_a$, i.e., $Q_{1,j}^{(n)} = Q_{M+1,j}^{(n)} = 1$; (ii) in θ–direction, p is periodic, i.e., $Q_{i,1}^{(n)} = Q_{i,N+1}^{(n)}$.

The computational algorithm using MATLAB is described in Flowchart 1. Application of an implicit finite–difference method (IFDM) on a one–dimensional problem, say $Q = f(\xi, \tau)$, results in a tridiagonal form of algebraic equations involving only three unknowns, $Q_{i+1}^{(n+1)}$, $Q_i^{(n+1)}$, and $Q_{i-1}^{(n+1)}$. Thomas' algorithm[34] can be used to solve these equations. When Eq. (8) is solved using an implicit method, there would be five unknowns, $Q_{i+1,j}^{(n+1)}$, $Q_{i,j}^{(n+1)}$, $Q_{i-1,j}^{(n+1)}$, $Q_{i,j+1}^{(n+1)}$, and $Q_{i,j-1}^{(n+1)}$. Due to the additional two unknowns $Q_{i,j+1}^{(n+1)}$, and $Q_{i,j-1}^{(n+1)}$, application of IFDM does not result in a tridiagonal form of algebraic equations, and hence Thomas' algorithm cannot be used directly in the solution procedure. Thomas' algorithm is preferred over the

other matrix solution methods as it saves computing time. Equation (8) is solved by using the Alternating–Direction Implicit (ADI) finite–difference method[7,16] to compute p field of airflow through AB. The ADI method splits the solution over a given time interval $\Delta\tau$ into two equal time–steps. In the first step, Q is implicitly written with respect to θ, and in the second step, Q is implicitly written with respect to ξ. The ADI finite–difference equation involves only three unknowns of Q at a given time–step, either in θ or in ξ direction. The first step of the ADI method results in the periodic tridiagonal form of algebraic equations. The second step of the ADI method results in the tridiagonal form of algebraic equations. Hence, Thomas' algorithm can be used only in the second step of the solution procedure. In the first step, a symbolic Thomas algorithm[35] is used. At the end of the two–step process, Q is marched over $\Delta\tau$. Equations (10) and (11) are solved along with Eqs (8) and (9).

During SSS, the trial value of the position $\left(e_J^0, \alpha_J^0\right)$ is assumed (see Fig. 3) in terms of $H_{i,j}^0$ using Eq. (9). ω of the journal and $\left(X_J(0), Y_J(0)\right)$ are specified. Using Eqs (8)–(11) (excluding the transient terms), the p–distribution around the journal is computed by the ADI approach, and integrated to find the static LCC $\left(F_J^{(x)}(0), F_J^{(y)}(0)\right)$. Since the position of CG_J is arbitrary to start with, the fluid forces do not balance P_R. Several trials with different positions of CG_J are needed to arrive at the correct candidate position $\left(e_J^0, \alpha_J^0\right)$ at which $F_J^{(y)}(0) \cong P_R$. In terms of force components $F^{(R)}$ along, and $F^{(T)}$ perpendicular to the line of centers, $\alpha_J^0 \cong \tan^{-1}\left|F_J^{(T)}/F_J^{(R)}\right|$ (see Fig. 3). Computations of force components are performed to an accuracy of ± 0.17% to P_R. The SSS provides $\left(e_J^0, \alpha_J^0\right)$ and $\left(F_J^{(T)}(0), F_J^{(R)}(0)\right)$ at various values of ω of the journal.

MATLAB code is written: (a) to define boundary conditions on the journal during TSS; and (b) to write out the time series of (X_J, Y_J), and $\left(\dot{X}_J, \dot{Y}_J\right)$. At each time–step during TSS, the motion of CG_J modifies the AB region according to Eq. (9). The velocity of moving nodes is computed as explained in the following Section.

Computation of Air–Bearing Film Thickness

During the TSS of the 1–DOF analysis, to compute the p distribution in the AB region, the position of the CG_B is fixed, and the CG_J is simulated to follow a prescribed SHM.[7,10] The journal undergoes rotation as well as translation. The TSS consists of two stages. A sub–routine is written in MATLAB that prescribes the translation of CG_J as $x_J = A\sin(\nu t)$ during stage–1 and $y_J = A\sin(\nu t)$ during stage–2 of TSS. Inputs for this sub-routine are $X_J(0)$, $Y_J(0)$, A, and ν. As TSS progresses, the spatial position of CG_J is computed by this sub–routine and is transferred (in terms of the dimensionless AB film thickness $H_{i,j}^{(n)}$) to the sub–routine that computes p using the ADI approach. Since the CG_B does not move, the motion of nodes on the bushing is not considered.

During stage–1 of TSS, the SHM can be written in discrete form as

$$x_J^{(n)} = A\sin\left((n-1)\Delta\tau\right), y_J^{(n)} = 0 \qquad \ldots(12)$$

where, $A \leq 0.3\ c_{AB}$ and $\Delta\tau = \nu\Delta t$.[7] Using Eq. (12), the eccentricity ratio $\epsilon_J^{(n)} = \sqrt{\left(X_J^{(n)}\right)^2 + \left(Y_J^{(n)}\right)^2}/c_{AB}$ during stage–1 of the TSS is

$$\epsilon_J^{(n)} = \sqrt{\left(e_J^0\sin\alpha_J^0 + A\sin\left((n-1)\Delta\tau\right)\right)^2 + \left(e_J^0\cos\alpha_J^0\right)^2}/c_{AB} \qquad \ldots(13)$$

During stage–2 of TSS, the SHM can be written in discrete form as $x_J^{(n)} = 0, y_J^{(n)} = A\sin\left((n-1)\Delta\tau\right)$. From Fig. 3, $X_J^{(n)} = e_J^0\sin\alpha_J^0$ and $Y_J^{(n)} = -e_J^0\cos\alpha_J^0 + A\sin\left((n-1)\Delta\tau\right)$. Hence,

$$\epsilon_J^{(n)} = \sqrt{\left(e_J^0\sin\alpha_J^0\right)^2 + \left(-e_J^0\cos\alpha_J^0 + A\sin\left((n-1)\Delta\tau\right)\right)^2}/c_{AB} \qquad \ldots(14)$$

H is arrived at using Eq. (9) as

$$H_{i,j}^{(n)} = 1 + \epsilon_J^{(n)}\cos[(j-1)\Delta\theta] \qquad \ldots(15)$$

During an SSS, $\epsilon_J = e_J^0/c_{AB}$. The translation of CG_J during a TSS is defined using $H_{i,j}^{(n)}$. ω of the journal is defined in terms of Λ at each time–step. When $H_{i,j}^{(n)}$ and Λ are implemented in Eq (8), the p–distribution can be computed by MATLAB. Integrating the p–distribution over the journal, $F_J^{(xx)}$ and $F_J^{(yx)}$ for stage–1 and $F_J^{(xy)}$ and $F_J^{(yy)}$ for stage–2, are computed at each time–step.

Alternating–Direction Implicit Method

Both the SSS and the TSS are carried out using the ADI approach. In the SSS, an iteration is discretized

into three levels, n, n+1, and n+2. In the TSS, a dimensionless time–step, $\Delta\tau$ is discretized into three levels: τ_n, τ_{n+1} and τ_{n+2}. Computations over a single iteration in the SSS and a single time–step $\Delta\tau$ in the TSS involve finding the solutions of Q at the levels n+1 and n+2. The solution of Q at the level n = 1 is known from the prescribed initial conditions during the first time–step, and the solution of Q at the level n is known from the computed Q at the level n+2 during the following time–steps. The static equilibrium conditions arrived at during SSS are used as initial conditions for TSS.

For conducting a TSS, $P_{i,j}(\tau = 0)$ and $H_{i,j}(\tau = 0)$ obtained from an SSS are used as initial conditions at level n = 1. The solution of Q is a two–step process, where intermediate values of Q are found at an intermediate iteration level, n+1 during an SSS and an intermediate time, τ+($\Delta\tau$/2) during a TSS, as follows. It is assumed that the p distribution in level n is known, at the beginning of the computations. In the first step over a time interval $\Delta\tau$/2, for the level n+1, Q in the derivatives with respect to θ in Eq. (8) are written as the unknowns. Q in the derivatives with respect to ξ are considered to be the known values from the level n resulting in Eq. (16).

$$
\begin{aligned}
&-\left(H_{i,j}^{(n)}\right)^3 \frac{Q_{i,j+1}^{(n+1)} - 2Q_{i,j}^{(n+1)} + Q_{i,j-1}^{(n+1)}}{(\Delta\theta)^2} \\
&- \left(H_{i,j}^{(n)}\right)^3 \frac{Q_{i+1,j}^{(n)} - 2Q_{i,j}^{(n)} + Q_{i-1,j}^{(n)}}{(\Delta\xi)^2} \\
&- 3\left(H_{i,j}^{(n)}\right)^2 \frac{\left(H_{i,j+1}^{(n)} - H_{i,j-1}^{(n)}\right)\left(Q_{i,j+1}^{(n+1)} - Q_{i,j-1}^{(n+1)}\right)}{4(\Delta\theta)^2} \\
&- 3\left(H_{i,j}^{(n)}\right)^2 \frac{\left(H_{i+1,j}^{(n)} - H_{i-1,j}^{(n)}\right)\left(Q_{i+1,j}^{(n)} - Q_{i-1,j}^{(n)}\right)}{4(\Delta\xi)^2} \\
&+ \Lambda \frac{H_{i,j}^{(n)}}{P_{i,j}^{(n)}} \frac{Q_{i,j+1}^{(n+1)} - Q_{i,j-1}^{(n+1)}}{2\Delta\theta} + 2\Lambda \frac{Q_{i,j}^{(n+1)}}{P_{i,j}^{(n)}} \frac{H_{i,j+1}^{(n)} - H_{i,j-1}^{(n)}}{2\Delta\theta} \\
&+ \lambda \frac{H_{i,j}^{(n)}}{P_{i,j}^{(n)}} \frac{Q_{i,j}^{(n+1)} - Q_{i,j}^{(n)}}{\Delta\tau/2} + 2\lambda \frac{Q_{i,j}^{(n+1)}}{P_{i,j}^{(n)}} \frac{H_{i,j}^{(n+1)} - H_{i,j}^{(n)}}{\Delta\tau/2} \\
&= \frac{\mathrm{C}_3 \upsilon_{\mathrm{FH}} \left(H_{i,j}^{\mathrm{FH}}\right)^{(n)} \pi_{\mathrm{FH}}}{\mathrm{C}_1 \Delta\theta\Delta\xi} \qquad \text{n} \quad \ldots(16)
\end{aligned}
$$

where, the unknowns are $Q_{i,j-1}^{(n+1)}, Q_{i,j}^{(n+1)}$, and $Q_{i,j+1}^{(n+1)}$ for $1 \le j \le N$ and $2 \le i \le M$. For each i, Eq. (16) reduces to the periodic tridiagonal matrix form

$$[\mathrm{A}][\mathrm{Q}] = [\mathrm{B}] \qquad \ldots(17)$$

Equation (17) in the expanded form is

$$
\begin{bmatrix}
b_{i,1} & c_{i,2} & 0 & 0 & \ldots & 0 & 0 & 0 & a_{i,N} \\
a_{i,1} & b_{i,2} & c_{i,3} & 0 & \ldots & 0 & 0 & 0 & 0 \\
0 & a_{i,2} & b_{i,3} & c_{i,4} & \ldots & 0 & 0 & 0 & 0 \\
\vdots & \vdots & \ddots & \ddots & \ddots & \ddots & \ddots & \vdots & \vdots \\
0 & 0 & 0 & 0 & \ldots & a_{i,N-3} & b_{i,N-2} & c_{i,N-1} & 0 \\
0 & 0 & 0 & 0 & \ldots & 0 & a_{i,N-2} & b_{i,N-1} & c_{i,N} \\
c_{i,1} & 0 & 0 & 0 & \ldots & 0 & 0 & a_{i,N-1} & b_{i,N}
\end{bmatrix}
\begin{bmatrix}
Q_{i,1}^{(n+1)} \\ Q_{i,2}^{(n+1)} \\ Q_{i,3}^{(n+1)} \\ \vdots \\ Q_{i,N-2}^{(n+1)} \\ Q_{i,N-1}^{(n+1)} \\ Q_{i,N}^{(n+1)}
\end{bmatrix}
=
\begin{bmatrix}
B_{i,1} \\ B_{i,2} \\ B_{i,3} \\ \vdots \\ B_{i,N-2} \\ B_{i,N-1} \\ B_{i,N}
\end{bmatrix}
$$

where,

$$
\begin{aligned}
a_{i,j} &= -\frac{\left(H_{i,j}^{(n)}\right)^3}{(\Delta\theta)^2} + 3\frac{\left(H_{i,j}^{(n)}\right)^2}{4(\Delta\theta)^2}\left(H_{i,j+1}^{(n)} - H_{i,j-1}^{(n)}\right) \\
&\quad - \Lambda \frac{H_{i,j}^{(n)}}{2P_{i,j}^{(n)}\Delta\theta}; \\
b_{i,j} &= \frac{2\left(H_{i,j}^{(n)}\right)^3}{(\Delta\theta)^2} + \frac{2\Lambda}{P_{i,j}^{(n)}} \frac{\left(H_{i,j+1}^{(n)} - H_{i,j-1}^{(n)}\right)}{2\Delta\theta} + \lambda \frac{H_{i,j}^{(n)}}{P_{i,j}^{(n)}\Delta\tau/2} \\
&\quad + 2\lambda \frac{\left(H_{i,j}^{(n+1)} - H_{i,j}^{(n)}\right)}{P_{i,j}^{(n)}\Delta\tau/2}; \\
c_{i,j} &= -\frac{\left(H_{i,j}^{(n)}\right)^3}{(\Delta\theta)^2} - 3\frac{\left(H_{i,j}^{(n)}\right)^2}{4(\Delta\theta)^2}\left(H_{i,j+1}^{(n)} - H_{i,j-1}^{(n)}\right) \\
&\quad + \Lambda \frac{H_{i,j}^{(n)}}{2P_{i,j}^{(n)}\Delta\theta}.
\end{aligned}
$$

and

At the grid points where the FH are located,

$$
\begin{aligned}
B_{i,j} &= \left(H_{i,j}^{(n)}\right)^3 \frac{\left(Q_{i+1,j}^{(n)} - 2Q_{i,j}^{(n)} + Q_{i-1,j}^{(n)}\right)}{(\Delta\xi)^2} + \\
&3\left(H_{i,j}^{(n)}\right)^2 \frac{\left(H_{i+1,j}^{(n)} - H_{i-1,j}^{(n)}\right)\left(Q_{i+1,j}^{(n)} - Q_{i-1,j}^{(n)}\right)}{4(\Delta\xi)^2} + \lambda \frac{H_{i,j}^{(n)}}{P_{i,j}^{n}} \frac{Q_{i,j}^{(n)}}{\Delta\tau/2} \\
&\quad + \frac{\mathrm{C}_3 \upsilon_{\mathrm{FH}} \left(H_{i,j}^{\mathrm{FH}}\right)^{(n)} \pi_{\mathrm{FH}}}{\mathrm{C}_1 \Delta\theta\Delta\xi}
\end{aligned}
$$

The last term in B_j would be zero for the case of grid points other than the location of FH.

$$
\begin{aligned}
Q_{i,0}^{(n+1)} &= Q_{i,N}^{(n+1)} \\
Q_{i,N+1}^{(n+1)} &= Q_{i,1}^{(n+1)}
\end{aligned}
$$

Equation (16) is used in a TSS. In order to carry out SSS, the terms containing $\Delta\tau$ in Eq. (16) are excluded. Equation (17) yields a solution for $Q_{i,j}^{(n+1)}$ for all j, keeping i fixed, using the symbolic Thomas

algorithm (see Appendix). That is, examining Fig. 5, at a fixed value of i, "sweeps" can be made in the θ direction, using Eq. (17) to solve for $Q_{i,j}^{(n+1)}$ for all values of j. Since there are N number of interior grid points in the θ direction, a sweep is made from $j = 1$ to N. This sweep utilizes the symbolic Thomas algorithm once. This computation is then repeated at the next row of grid points designated by $i + 1$. i.e., i in Eq. (17) is replaced by $i + 1$ and solved for $Q_{i+1,j}^{(n+1)}$. Since there are M–1 number of interior grid points in the ξ direction, this process is repeated M–1 times; i.e., there are M–1 sweeps in the θ direction, resulting in the symbolic Thomas algorithm being used M–1 times. At the end of this step, the values of Q, at the intermediate iteration level n+1 in an SSS and at the intermediate time τ+($\Delta\tau$/2) in a TSS, are known at all grid points (i, j); i.e., $Q_{i,j}^{(n+1)}$ is known at all (i, j).

In the second step, for the level n+2, Q in the derivatives with respect to ξ are the unknowns, and the derivatives with respect to θ are computed using the known values Q from the level n+1. The second step of the ADI scheme takes the solution to the iteration n+2 in an SSS and to the time $\tau + \Delta\tau$ in a TSS, using the known values at the iteration level n+1 in an SSS and the time $\tau + (\Delta\tau/2)$ in a TSS. For this second step, Eq. (8) becomes

$$-\left(H_{i,j}^{(n+1)}\right)^3 \frac{Q_{i,j+1}^{(n+1)} - 2Q_{i,j}^{(n+1)} + Q_{i,j-1}^{(n+1)}}{(\Delta\theta)^2} - \left(H_{i,j}^{(n+1)}\right)^3 \frac{Q_{i+1,j}^{(n+2)} - 2Q_{i,j}^{(n+2)} + Q_{i-1,j}^{(n+2)}}{(\Delta\xi)^2} - 3\left(H_{i,j}^{(n+1)}\right)^2 \frac{\left(H_{i,j+1}^{(n+1)} - H_{i,j-1}^{(n+1)}\right)\left(Q_{i,j+1}^{(n+1)} - Q_{i,j-1}^{(n+1)}\right)}{4(\Delta\theta)^2} - 3\left(H_{i,j}^{(n+1)}\right)^2 \frac{\left(H_{i+1,j}^{(n+1)} - H_{i-1,j}^{(n+1)}\right)\left(Q_{i+1,j}^{(n+2)} - Q_{i-1,j}^{(n+2)}\right)}{4(\Delta\xi)^2} + \Lambda \frac{H_{i,j}^{(n+1)}}{P_{i,j}^{(n+1)}} \frac{Q_{i,j+1}^{(n+1)} - Q_{i,j-1}^{(n+1)}}{2\Delta\theta} + 2\Lambda \frac{Q_{i,j}^{(n+2)}}{P_{i,j}^{(n+1)}} \frac{H_{i,j+1}^{(n+1)} - H_{i,j-1}^{(n+1)}}{2\Delta\theta} + \lambda \frac{H_{i,j}^{(n+1)}}{P_{i,j}^{(n+1)}} \frac{Q_{i,j}^{(n+2)} - Q_{i,j}^{(n+1)}}{\Delta\tau/2} + 2\lambda \frac{Q_{i,j}^{(n+2)}}{P_{i,j}^{(n+1)}} \frac{H_{i,j}^{(n+2)} - H_{i,j}^{(n+1)}}{\Delta\tau/2} = \frac{C_3 \upsilon_{FH} \left(H_{i,j}^{FH}\right)^{(n+1)} \pi_{FH}}{C_1 \Delta\theta \Delta\xi} \quad \ldots (18)$$

where, the unknowns are $Q_{i-1,j}^{(n+2)}, Q_{i,j}^{(n+2)}, and\ Q_{i+1,j}^{(n+2)}$ for $2 \le i \le M$ and $1 \le j \le N$. Equation (18) reduces to the tridiagonal matrix form for each j:

$$[A][Q] = [B] \quad \ldots (19)$$

Equation (19) in the expanded form is

$$\begin{bmatrix} b & c & 0 & 0 & \ldots & 0 & 0 & 0 & 0 \\ a & b & c & 0 & \ldots & 0 & 0 & 0 & 0 \\ 0 & a & b & c & \ldots & 0 & 0 & 0 & 0 \\ \vdots & \vdots & \ddots & \ddots & \ddots & \ddots & \ddots & \vdots & \vdots \\ 0 & 0 & 0 & 0 & \ldots & a & b & c & 0 \\ 0 & 0 & 0 & 0 & \ldots & 0 & a & b & c \\ 0 & 0 & 0 & 0 & \ldots & 0 & 0 & a & b \end{bmatrix} \begin{bmatrix} Q_{2,j}^{(n+2)} \\ Q_{3,j}^{(n+2)} \\ Q_{4,j}^{(n+2)} \\ \vdots \\ Q_{M-2,j}^{(n+2)} \\ Q_{M-1,j}^{(n+2)} \\ Q_{M,j}^{(n+2)} \end{bmatrix} = \begin{bmatrix} B_2' \\ B_3 \\ B_4 \\ \vdots \\ B_{M-2} \\ B_{M-1} \\ B_M' \end{bmatrix}$$

where,

$$a = -\frac{\left(H_{i,j}^{(n+1)}\right)^3}{(\Delta\xi)^2} + 3\frac{\left(H_{i,j}^{(n+1)}\right)^2}{4(\Delta\xi)^2}\left(H_{i+1,j}^{(n+1)} - H_{i-1,j}^{(n+1)}\right);$$

$$b = \frac{2\left(H_{i,j}^{(n+1)}\right)^3}{(\Delta\xi)^2} + 2\Lambda \frac{1}{P_{i,j}^{(n+1)}} \frac{H_{i,j+1}^{(n+1)} - H_{i,j-1}^{(n+1)}}{2\Delta\theta} + \lambda \frac{H_{i,j}^{(n+1)}}{P_{i,j}^{(n+1)}\,\Delta\tau/2} + 2\lambda \frac{\left(H_{i,j}^{(n+2)} - H_{i,j}^{(n+1)}\right)}{P_{i,j}^{(n+1)}\,\Delta\tau/2};$$

and

$$c = -\frac{\left(H_{i,j}^{(n+1)}\right)^3}{(\Delta\xi)^2} - 3\frac{\left(H_{i,j}^{(n+1)}\right)^2}{4(\Delta\xi)^2}\left(H_{i+1,j}^{(n+1)} - H_{i-1,j}^{(n+1)}\right).$$

At the grid points where the FH are located,

$$B_j = \left(H_{i,j}^{(n+1)}\right)^3 \frac{Q_{i,j+1}^{(n+1)} - 2Q_{i,j}^{(n+1)} + Q_{i,j-1}^{(n+1)}}{(\Delta\theta)^2} + 3\left(H_{i,j}^{(n+1)}\right)^2 \frac{\left(H_{i,j+1}^{(n+1)} - H_{i,j-1}^{(n+1)}\right)\left(Q_{i,j+1}^{(n+1)} - Q_{i,j-1}^{(n+1)}\right)}{4(\Delta\theta)^2} - \Lambda \frac{H_{i,j}^{(n+1)}}{P_{i,j}^{(n+1)}} \frac{Q_{i,j+1}^{(n+1)} - Q_{i,j-1}^{(n+1)}}{2\Delta\theta} + \lambda \frac{H_{i,j}^{(n+1)}}{P_{i,j}^{(n+1)}} \frac{Q_{i,j}^{(n+1)}}{\Delta\tau/2} + \frac{C_3 \upsilon_{FH} \left(H_{i,j}^{FH}\right)^{(n+1)} \pi_{FH}}{C_1 \Delta\theta \Delta\xi}$$

The last term in B_j would be zero for the case of grid points other than the location of FH.

$$B_2' = B_2 - aQ_{1,j}^{(n+2)}$$

$$B_M' = B_M - cQ_{M+1,j}^{(n+2)}$$

Equation (18) is used in a TSS. In order to carry out SSS, the terms containing $\Delta\tau$ in Eq. (18) are excluded. Equation (19) yields a solution for $Q_{i,j}^{(n+2)}$ for all i, keeping j fixed, using Thomas' algorithm.[34] That is, examining Fig. 5, at a fixed value of j, "sweeps" can be made in the ξ direction, using Eq. (19) to solve for $Q_{i,j}^{(n+2)}$ for all values of i. Since there are M–1 number of interior grid points in the ξ

direction, a sweep is made from i = 2 to M. This sweep utilizes Thomas' algorithm once. This computation is then repeated at the next column of grid points designated by j+1. i.e., j in Eq. (19) is replaced by j+1 and solved for $Q_{i,j+1}^{(n+2)}$ for all values of i from 2 to M, using Thomas' algorithm. Since there are N number of interior grid points in the θ direction, this process is repeated N times; i.e., there are N sweeps in the ξ direction, resulting in Thomas' algorithm being used N times. At the end of this step, the values of Q, at the iteration level n+2 in an SSS and at the time τ+ $\Delta\tau$ in a TSS, are known at all grid points (i, j); i.e., $Q_{i,j}^{(n+2)}$ is known at all (i, j). After the second step, the level n+2 is treated as a new level n, and the iteration marching in an SSS and the time marching in a TSS, are continued to n+4 and $\tau + 2\Delta\tau$, respectively, and so on. When $F_{\mathrm{J}}{}^{(x)}(0)\big|_{n+2} - F_{\mathrm{J}}{}^{(x)}(0)\big|_{n} < 0.001$ and $F_{\mathrm{J}}{}^{(y)}(0)\big|_{n+2} - F_{\mathrm{J}}{}^{(y)}(0)\big|_{n} < 0.001$, the iteration marching is stopped in the SSS. When $\tau = \tau_{\max}$, the time marching is stopped in the TSS. To improve the convergence of the force quantities during SSS, the relaxation of the Q variable is implemented using $Q_{i,j}^{(n+2)} \rightarrow \sigma Q_{i,j}^{(n+2)} + (1-\sigma)Q_{i,j}^{(n)}$ where the relaxation variable σ is assumed in the range of $0 < \sigma < 1$.[36]

Computation of Dynamic Load–Carrying Capacity

Equations (8)–(11) are used to compute the p distribution in the AB. It is shown in the literature[14,16] that in the case of an infinite length bearing, the contribution of shear stress distribution towards the load P_{R} is tiny in comparison to the contribution from p distribution and, therefore, can be neglected. Hence, in evaluating the LCC of the finite–length bearing, knowledge of the p distribution inside the bearing would be sufficient. Using Eqs. (2)–(5), the components of the LCC of the AB, $F_{\mathrm{J}}^{(R)}$ along, and $F_{\mathrm{J}}^{(T)}$ perpendicular to the line of centers, are given below.

$$F_{\mathrm{J}}^{(R)} = -p_{\mathrm{a}} R_{\mathrm{J}}^2 \int_0^{2\pi} \int_0^{\frac{L}{R_{\mathrm{J}}}} P(\xi,\theta)\cos\theta \, d\xi d\theta \qquad \ldots(20)$$

$$F_{\mathrm{J}}^{(T)} = p_{\mathrm{a}} R_{\mathrm{J}}^2 \int_0^{2\pi} \int_0^{\frac{L}{R_{\mathrm{J}}}} P(\xi,\theta)\sin\theta \, d\xi d\theta \qquad \ldots(21)$$

The average P is obtained by dividing the sum of $P_{i,j}$ values taken over all grid points by the total number of grid points. The dynamic LCC of the AB is computed by multiplying the average p with the surface area.

$$F_{\mathrm{J}}^{(R)}(n+2) = -\left[\sum_{i=1}^{i=M+1}\sum_{j=1}^{j=N} P_{ij}^{n+2}\cos\big((j-1)\Delta\theta\big)\right]\frac{2\pi p_{\mathrm{a}} L R_{\mathrm{J}}}{(M+1)N} \qquad \ldots(22)$$

$$F_{\mathrm{J}}^{(T)}(n+2) = \left[\sum_{i=1}^{i=M+1}\sum_{j=1}^{j=N} P_{ij}^{n+2}\sin\big((j-1)\Delta\theta\big)\right]\frac{2\pi p_{\mathrm{a}} L R_{\mathrm{J}}}{(M+1)N} \qquad \ldots(23)$$

Referring to Fig. 3 and using Eqs (24) and (25), $F_{\mathrm{J}}^{(x)}(t)$ and $F_{\mathrm{J}}^{(y)}(t)$ can be obtained from $F_{\mathrm{J}}^{(R)}(t)$ and $F_{\mathrm{J}}^{(T)}(t)$.

$$F_{\mathrm{J}}^{(T)}(t) = F_{\mathrm{J}}^{(x)}(t)\cos\alpha_{\mathrm{J}}^0 + F_{\mathrm{J}}^{(y)}(t)\sin\alpha_{\mathrm{J}}^0 \qquad \ldots(24)$$

$$F_{\mathrm{J}}^{(R)}(t) = -F_{\mathrm{J}}^{(x)}(t)\sin\alpha_{\mathrm{J}}^0 + F_{\mathrm{J}}^{(y)}(t)\cos\alpha_{\mathrm{J}}^0 \qquad \ldots(25)$$

Components of incremental dynamic LCC are obtained using the components of static LCC for the journal, $\left(F_{\mathrm{J}}^{(x)}(0), F_{\mathrm{J}}^{(y)}(0)\right)$ as

$$f_{\mathrm{J}}^{(x)}(t) = F_{\mathrm{J}}^{(x)}(t) - F_{\mathrm{J}}^{(x)}(0) \qquad \ldots(26)$$

$$f_{\mathrm{J}}^{(y)}(t) = F_{\mathrm{J}}^{(y)}(t) - F_{\mathrm{J}}^{(y)}(0) \qquad \ldots(27)$$

Computation of Dynamic Characteristics of Air–Bearing

The journal center is simulated to follow an SHM as defined in Eq. (12) to determine the DC. Such a simulation, conducted with a specified time–step Δt, provide data for calculations of the stiffness coefficients $K_{\mathrm{AB}}^{(ij)}$ and the damping coefficients $C_{\mathrm{AB}}^{(ij)}$, in the form of the following vectors of displacements $\mathrm{x_J}$, $\mathrm{y_J}$; velocities $\dot{\mathrm{x}}_{\mathrm{J}}$, $\dot{\mathrm{y}}_{\mathrm{J}}$; and forces $\mathrm{f}_{\mathrm{J}}^{(xx)}, \mathrm{f}_{\mathrm{J}}^{(yx)}, \mathrm{f}_{\mathrm{J}}^{(xy)}$, and $\mathrm{f}_{\mathrm{J}}^{(yy)}$. There are N+1 elements in $\mathrm{x_J}$, i.e., $\mathrm{x_J}(t_n) = \{x_{\mathrm{J}}(t_0), x_{\mathrm{J}}(t_1), x_{\mathrm{J}}(t_2), \ldots x_{\mathrm{J}}(t_N)\}$, where $t_n = n\Delta t$ and n = 0, 1, 2,…, N. Velocity $\dot{\mathrm{x}}_{\mathrm{J}}$ can then be found from $\mathrm{x_J}$ by time–differentiation. Similar N+1 elements can be envisaged for $\mathrm{y_J}, \dot{\mathrm{y}}_{\mathrm{J}}, \mathrm{f}_{\mathrm{J}}^{(xx)}, \mathrm{f}_{\mathrm{J}}^{(yx)}, \mathrm{f}_{\mathrm{J}}^{(xy)}$, and $\mathrm{f}_{\mathrm{J}}^{(yy)}$. These vectors satisfy the relations: $\mathrm{f}_{\mathrm{J}}^{(xx)} = C_{\mathrm{AB}}^{(xx)}\dot{\mathrm{x}}_{\mathrm{J}} + K_{\mathrm{AB}}^{(xx)}\mathrm{x_J}$, $\mathrm{f}_{\mathrm{J}}^{(yx)} = C_{\mathrm{AB}}^{(yx)}\dot{\mathrm{x}}_{\mathrm{J}} + K_{\mathrm{AB}}^{(yx)}\mathrm{x_J}$, $\mathrm{f}_{\mathrm{J}}^{(xy)} =$

$C_{AB}^{(xy)}\dot{y}_J + K_{AB}^{(xy)}y_J$, $f_J^{(yy)} = C_{AB}^{(yy)}\dot{y}_J + K_{AB}^{(yy)}y_J$. The $K^{(ij)}$ and $C^{(ij)}$ are calculated using the Gram–Schmidt orthogonalization process, as explained in the literature.[15,16]

The mesh sensitivity of the numerical solution is studied by estimating: (a) spatial discretization error, and (b) temporal discretization error. It is done by following the procedure given in the literature.[15,16,37] The error E_i due to spatial discretization is estimated by carrying out SSS with ω = 6623.6 rad s^{-1} and ϵ_J^0 = 0.2293 at three successively refined grid levels. M and N of the computational grid shown in Fig. 5 are varied to define three different grid levels: (16 × 32), (32 × 64), and (64 × 128), in the experiments. During TSS, the E_i due to the temporal discretization is estimated with ω = 6623.6 rad s^{-1} and $v = \omega/2$, for three different time periods Δt: $(\Delta t)_1 = T/1800$, $(\Delta t)_2 = T/3600$, and $(\Delta t)_3 = T/7200$, where the period of vibration is $T = 2\pi/v$. The results of mesh sensitivity are given in Tables 1 and 2. Except for $U = F_J^{(T)}(0)$ in Table 1, there is a monotonic reduction of E_i for each of the measured U at successively refined grid levels. In this research, the entire SSS and TSS are carried out using spatial grid level 3 and temporal grid level 3, to improve the numerical accuracy due to the finest grid and the smallest Δt. The grid convergence indicator GCI_3 calculated at grid level 3, gives the degree of confidence in the results of the 1–DOF approach presented in this paper. For example, referring to Table 2, $K_{AB}^{(xx)}$= 1.3514 × 10^8± 3.4088 × 10^7 N m^{-1}.

Results and Discussion

Design of rotor–journal bearing systems usually involves a static analysis and a dynamic analysis. In a static analysis, the designer is interested in finding the equilibrium position of the journal. The static characteristics, such as eccentricity ratio and attitude angle, define the equilibrium position of the journal. The dynamic analysis yields characteristics such as stiffness coefficients and damping coefficients of a bearing, which can then be used to carryout analysis for critical speed and stability of rotor–bearing system. The objective is to study and analyze a rotor–journal AB system. Analysis has been carried out by mathematical modeling and numerical simulation of its dynamic motion as explained in the Section–Materials and Methods. The entire mathematical procedure is coded in MATLAB software. The results of the static and dynamic analyses done on AB are presented in the following section.

Pressure Distribution in the Air–Bearing

The data in Fig. 7 shows the p–distribution in the AB when ω = 6623.6 rad s^{-1} and when the CG_J is at its SEP. This data is obtained by solving Eqs(16) and (18) during SSS. It is observed from this figure that p at both ends of the bearing is atmospheric, thereby satisfying the imposed boundary condition, while the p–distribution in the θ direction is continuous. There are 16 grid points where p is observed to attain a peak value. These grid points correspond to the locations where the FH are present. Due to the drop in p as the air flows through the FH, p at the grid points corresponding to locations of FH are observed to be

Table 1 — Estimation of spatial discretization error

	U_1	U_2	U_3	λ	E_1	E_2	E_3	GCI_3
$F_J^{(R)}(0)$ (N)	1068.73	1106.25	1114.56	2.17	48.20	10.68	2.37	7.10
$F_J^{(T)}(0)$ (N)	–104.55	–99.55	–93.62	–0.25	–26.91	–31.91	–37.84	–113.52
$F_J^{(y)}(0)$ (N)	1073.83	1110.72	1118.49	2.25	46.73	9.84	2.07	6.22
α_J^0 (rad)	–0.0975	–0.0897	–0.0838	0.39	0.0331	0.0253	0.0194	0.0582

Table 2 — Estimation of temporal discretization error

	U_1 10^8 (N m^{-1})	U_2 10^8 (N m^{-1})	U_3 10^8 (N m^{-1})	λ	E_1 10^7 (N m^{-1})	E_2 10^7 (N m^{-1})	E_3 10^7 (N m^{-1})	GCI_3 10^7 (N m^{-1})
$K_{AB}^{(xx)}$	1.4213	1.3822	1.3514	0.3458	–1.8351	–1.444	–1.1363	–3.4088
$K_{AB}^{(xy)}$	0.2217	0.3073	0.347	1.1092	1.596	0.7398	0.3429	1.0288
	U_1 10^3 (N s m^{-1})	U_2 10^3 (N s m^{-1})	U_3 10^3 (N s m^{-1})	λ	E_1 10^3 (N s m^{-1})	E_2 10^3 (N s m^{-1})	E_3 10^3 (N s m^{-1})	GCI_3 10^3 (N s m^{-1})
$C_{AB}^{(xx)}$	–5.9897	–5.7191	–5.6522	2.0161	0.3595	0.0889	0.022	0.0659
$C_{AB}^{(xy)}$	–5.6217	–5.2575	–5.4531	0.897	0.237	–0.1273	0.0683	0.205

less than the specified p_s = 7 bar. Along the z direction, the p–distribution is uniform between locations of FH but decreases to p_a at the bearing ends. It indicates that air flows from the locations of FH towards the bearing ends along the z–direction. Since the CG_J is at its SEP, the p–distribution in Fig. 7 varies around the circumference and has its maximum value at θ = 3.0578 rad that corresponds to α_J^0 = –0.0838 rad at ω = 6623.6 rad s^{-1}. In reality, this condition corresponds to a stable steady–state operating condition of the journal.

Pressure Distribution in Feed–Hole Chambers and Mass Flow Rate of Air Through Feed–Holes of Air–Bearing

The data in Fig. 8 shows the variations of FH chamber pressure (p_c) with t when the journal rotates at ω = 6623.6 rad s^{-1} with the vibrational frequency of CG_J, v = 3311.8 rad s^{-1}. The data in Fig. 8(a) shows the variations of p_c in the $((M/4)+1)^{th}$ row of FH (see Fig. 5) from 1 to 4. The data in Fig. 8(b) shows the variations of p_c in FH from 5 to 8. The location of FH_1 is at θ = 0 rad (see Fig. 5). The data in Fig. 9 shows the mass flow rate of air ($\dot{m}_{FH}$) through these FH. The data in Fig. 9(a) shows $\dot{m}_{FH}$ through FH from 1 to 4. The data in Fig. 9(b) shows $\dot{m}_{FH}$ through FH from 5 to 8.

There is a periodic variation in p_c as the CG_J executes an SHM along the y–direction. When the CG_J moves in y<0 direction, p in chambers 4, 5, and 6 increases, and p in chambers 1, 2, and 8 decreases, while the p in chambers 3 and 7 is not significantly affected by this CG_J motion. Hence, there is a decrease in $\dot{m}_{FH}$ through the FH_4, FH_5, and FH_6 and an increase in $\dot{m}_{FH}$ through FH_1, FH_2, and FH_8 while the $\dot{m}_{FH}$ through the FH_3 and FH_7 is not significantly affected by this motion. Similarly, it can be shown that p in chambers 6, 7, and 8 increases and p in chambers 2, 3, and 4 decreases while the p in chambers 1 and 5 is not affected when the CG_J executes motion in x>0 direction. Since the CG_J executes the SHM about its SEP (where the CG_J is below CG_B), the average p_c in FH_4, FH_5, and FH_6 is greater than the average p_c in FH_1, FH_2, FH_3, FH_7, and FH_8.

The maximum average p_c that exists at FH_5 is smaller than p_s = 7 bar as there is a drop in p from the air inlet to the FH chamber through the orifice (see Fig. 6). In Fig. 9, it is observed that $\dot{m}_{FH}$ in all the FH are smaller than the critical mass flow rate ($\dot{m}_{FH,cr}$). These results show that the flow through the FH is not hydrodynamically choked. p_c and $\dot{m}_{FH}$ are calculated using υ_{FH} and π_{FH}.

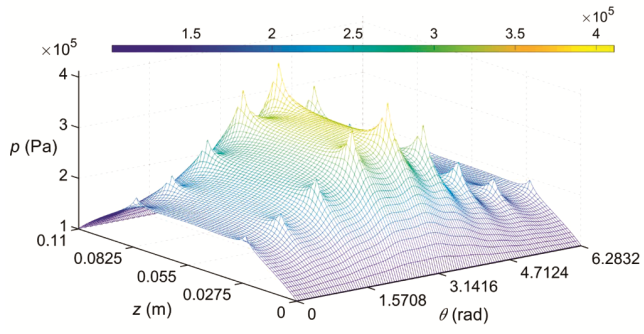

Fig. 7 — Pressure distribution in air–bearing (At static equilibrium position for angular velocity of journal ω = 6623.6 rad s^{-1} and supply air pressure p_s = 7 bar; Pressure peaks are at 16 feed–hole locations; Pressure decreases along flow direction from feed–hole locations to bearing ends; Pressure is atmospheric at bearing ends)

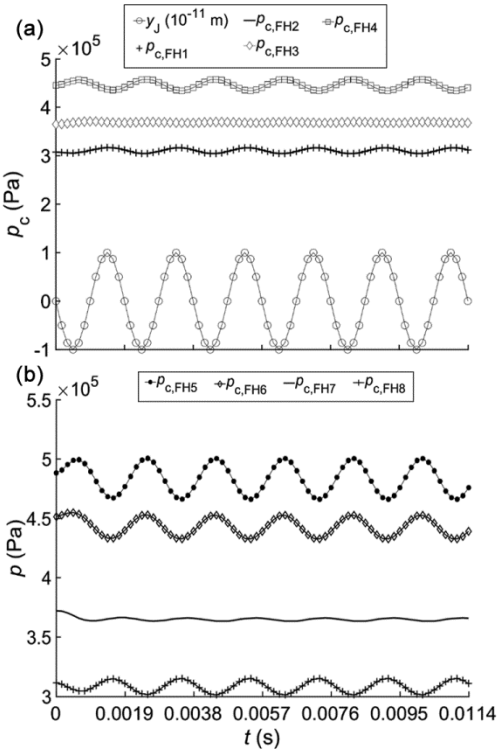

Fig. 8 — Pressure (p) distribution in feed–hole (FH) chambers (c) of air–bearing: (a) Feed–holes 1, 2, 3, and 4, (b) Feed–holes 5, 6, 7, and 8 (When the journal rotates at ω = 6623.6 rad s^{-1} and the journal center CG_J vibrates at $v = \omega/2$ in y direction; Since the center lines of FH_3 and FH_7 are along x direction, p_c in FH_3 and FH_7 are not significantly affected by journal motion; As the journal vibrates about its static equilibrium position where the CG_J is below the bushing center CG_B, the average p_c in FH_4, FH_5, and FH_6 are greater than the average p_c in FH_1, FH_2, FH_3, FH_7, and FH_8)

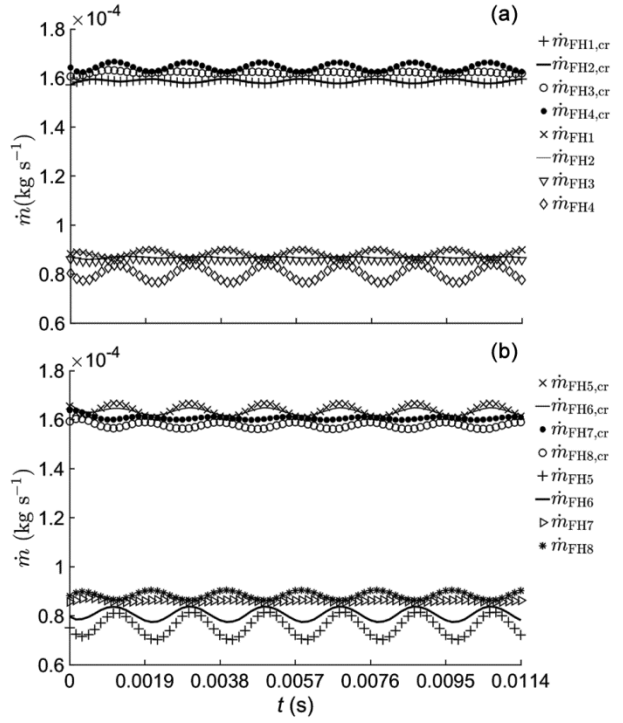

Fig. 9 — Mass flow rate ($\dot{m}_{FH}$) of air through feed–holes (FH) of air–bearing: (a) Feed–holes 1, 2, 3, and 4, (b) Feed–holes 5, 6, 7, and 8 (When the journal rotates at ω = 6623.6 rad s^{-1} and the journal center CG_J vibrates at $v = \omega/2$ in y direction; Since the center lines of FH_3 and FH_7 are along x direction, $\dot{m}_{FH}$ through the FH_3 and FH_7 are not significantly affected by journal motion; Results of $\dot{m}_{FH}$ smaller than the critical mass flow rate ($\dot{m}_{FH,cr}$) show that the flow through the FH is not hydrodynamically choked)

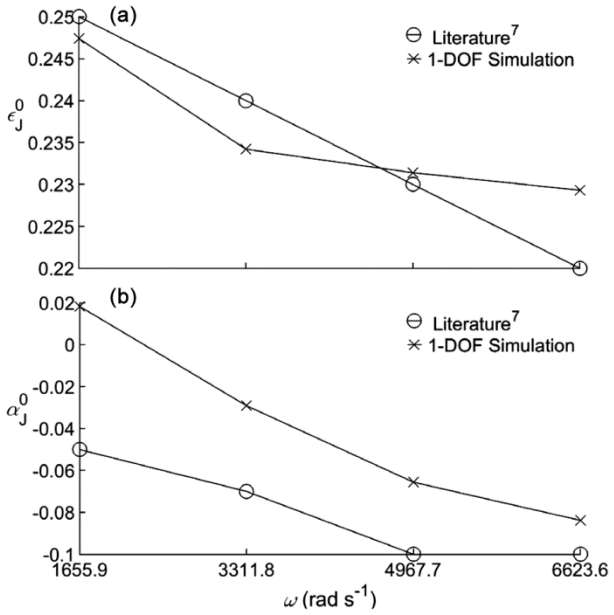

Fig. 10 — Static characteristics of AB: (a) Eccentricity ratio (ϵ_J^0), (b) Attitude angle (α_J^0) (Static equilibrium positions of the journal $(\epsilon_J^0, \alpha_J^0)$ arrived at various angular velocities of the journal ω; Static equilibrium positions are attained with decrease in ϵ_J^0 and α_J^0 as ω is increased; Negligibly small variations of ϵ_J^0 and α_J^0 show that the contribution of hydrostatic lubrication towards pressure development in AB is much greater than the contribution of hydrodynamic lubrication; ϵ_J^0 results from 1–DOF approach presented in this paper and ϵ_J^0 of literature[7] differ by 0.34%; Results of α_J^0 differ by 61.4%. Both predict a decrease in α_J^0 with an increase of ω)

Static Characteristics of Air–Bearing

The static characteristics solutions calculated using the 1–DOF approach are compared with the solutions given in the literature.[7] The comparisons are shown in Fig. 10. In Fig. 10(a), both the solutions show that with an increase in ω, there is a decrease in ϵ_J^0 of the CG_J to reach the SEP.[38] The ϵ_J^0 results from the 1–DOF approach and the ϵ_J^0 of the literature[7] differ by 0.34%, in an average sense. The data in Fig. 10(b) shows the results of α_J^0, for which the average difference between results of the 1–DOF approach and the literature[7] is 61.4%. Equations (8), (10), and (11) were obtained independently by applying the fundamental laws of mass, momentum, and energy to the flow models as discussed in Sections–*Governing equation for pressure distribution in air–bearing* and *Governing equations for mass flow through the feed–holes of air–bearing*. The average percentage difference in α_J^0 is attributed to the minor differences in the mathematical models used in this research and the literature.[7] It is observed that both the 1–DOF approach and the literature[7] predict a decrease in α_J^0 with an increase of ω. However, from Fig. 10, it is seen that the variations of ϵ_J^0 and α_J^0over the given range of ω are negligibly small. These results suggest that the role of hydrodynamic lubrication may be insignificant and the AB operates significantly under the hydrostatic lubrication mechanism due to the supply of externally–pressurized air.

Dynamic Load–Carrying Capacity

The data in Fig. 11 shows the incremental displacement $x_J(t)$ and the incremental dynamic LCC, $f_J^{(xx)}(t)$ and $f_J^{(yx)}(t)$ for AB. $f_J^{(xx)}(t)$ and $f_J^{(yx)}(t)$ are obtained using Eqs (26) and (27), respectively. These data are obtained by simulating the CG_J to follow an SHM along the x–direction. It is observed that there is a periodic variation in the values of force components after some initial transients, which shows that the bearing operation is

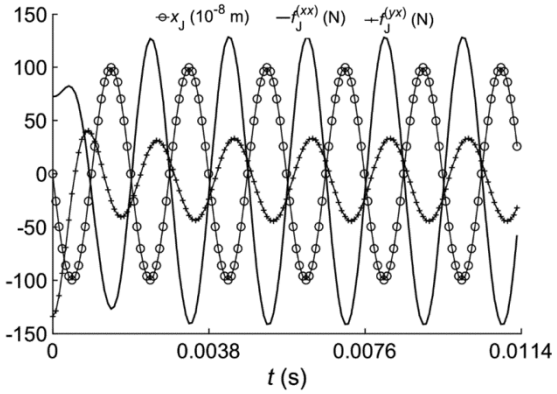

Fig. 11 — Incremental dynamic load–carrying capacity $f_{\mathrm{J}}^{(xx)}(t)$ and $f_{\mathrm{J}}^{(yx)}(t)$ of AB (When the journal rotates at ω = 6623.6 rad s^{-1} and $\mathrm{CG_J}$ executes a simple harmonic motionalong x–direction with $v = \omega/2$; $f_{\mathrm{J}}^{(xx)}(t)$ and $f_{\mathrm{J}}^{(yx)}(t)$ can be related to $f_{\mathrm{J}}^{(R)}(t)$ and $f_{\mathrm{J}}^{(T)}(t)$ which are used to determine stiffness coefficients and damping coefficients of AB; These dynamic characteristics dictate the dynamic stability of the AB)

at the steady–state condition. The time series of $x_{\mathrm{J}}(t)$, $f_{\mathrm{J}}^{(xx)}(t)$, and $f_{\mathrm{J}}^{(yx)}(t)$ are used to determine the DC using the orthogonalization process.

Since the AB is analyzed for a perfectly balanced rotor, at any given ω, the $\mathrm{CG_J}$ occupies a steady–state position or SEP defined by e_{J}^0 and α_{J}^0 (see Fig. 3). When the $\mathrm{CG_J}$ is at SEP, $F_{\mathrm{J}}^{(R)}(0), F_{\mathrm{J}}^{(T)}(0)$, and P_{R} are in equilibrium (see Section–*Mechanical equilibrium conditions in a loaded air–bearing*). The dynamic stability of the AB is concerned with the ability of the $\mathrm{CG_J}$ to return to this position after its excursion away from this position due to a disturbance when the rotor rotates at any given ω. At a given ω, for any position of the $\mathrm{CG_J}$ away from the SEP, $f_{\mathrm{J}}^{(R)}(t) = F_{\mathrm{J}}^{(R)}(t) - F_{\mathrm{J}}^{(R)}(0), f_{\mathrm{J}}^{(T)}(t) = F_{\mathrm{J}}^{(T)}(t) - F_{\mathrm{J}}^{(T)}(0)$ and $m_{\mathrm{R}}\mathbf{a}_{\mathrm{J}}(t)$ are in equilibrium, where acceleration of the journal $\mathbf{a}_{\mathrm{J}}(t)$ has components $a_{\mathrm{J}}^{(R)}$ along, and $a_{\mathrm{J}}^{(T)}$ perpendicular to the line of centers. At a given ω, for any position of the $\mathrm{CG_J}$ away from the SEP, $f_{\mathrm{J}}^{(R)}(t)$ and $f_{\mathrm{J}}^{(T)}(t)$ vary with v. For a given v, if $f_{\mathrm{J}}^{(R)}(t)$ and $f_{\mathrm{J}}^{(T)}(t)$ result in a motion of $\mathrm{CG_J}$ with a diminishing amplitude then the AB is said to be dynamically stable. For a given v, if $f_{\mathrm{J}}^{(R)}(t)$ and $f_{\mathrm{J}}^{(T)}(t)$ result in a motion of $\mathrm{CG_J}$ with an increasing amplitude then the AB is said to be dynamically unstable. The components of incremental dynamic LCC, $f_{\mathrm{J}}^{(R)}(t)$ and $f_{\mathrm{J}}^{(T)}(t)$ dictate the stability of the AB and not the components of static LCC, $F_{\mathrm{J}}^{(R)}(0)$ and $F_{\mathrm{J}}^{(T)}(0)$. Thus, it is $\dot{\alpha}_{\mathrm{J}}(t)$ and $\ddot{\alpha}_{\mathrm{J}}(t)$ and not α_{J}^0 that dictates the stability of the AB. The dynamic stability of the AB is not affected by the variation of the attitude angle, α_{J}^0. The components of incremental dynamic LCC, $f_{\mathrm{J}}^{(R)}(t)$ and $f_{\mathrm{J}}^{(T)}(t)$, are used to determine the DC such as stiffness coefficients and damping coefficients of AB. These DC of AB dictate the dynamic stability of the AB.

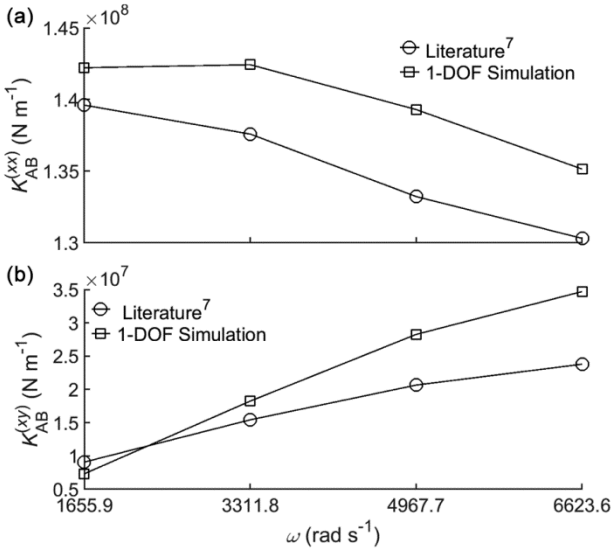

Fig. 12 — Dynamic characteristics of air–bearing: (a) Direct stiffness coefficients, (b) Cross–coupled stiffness coefficients (Dynamic characteristics calculated using 1–DOF approach and the literature[7] differ by 4.1%; $K_{\mathrm{AB}}^{(xy)}$ are 5–times smaller than $K_{\mathrm{AB}}^{(xx)}$; It implies that destabilizing effects associated with the hydrodynamic lubrication mechanism in AB are not negligible)

Dynamic Characteristics of Air–Bearing

The data in Figs 12 and 13 show the comparisons of the DC determined using the 1–DOF approach with the results given in the literature.[7] The results are shown as functions of ω. Due to the comparatively small journal eccentricity ε (e = 1–3 μm), the calculated values of the DC fulfill the following relations: $K_{\mathrm{AB}}^{(yy)} \approx K_{\mathrm{AB}}^{(xx)}, C_{\mathrm{AB}}^{(yy)} \approx C_{\mathrm{AB}}^{(xx)}, K_{\mathrm{AB}}^{(yx)} \approx -K_{\mathrm{AB}}^{(xy)}, C_{\mathrm{AB}}^{(yx)} \approx -C_{\mathrm{AB}}^{(xy)}$. Hence, a presentation of coefficients $K_{\mathrm{AB}}^{(yy)}, C_{\mathrm{AB}}^{(yy)}, K_{\mathrm{AB}}^{(yx)}$, and $C_{\mathrm{AB}}^{(yx)}$ has been avoided. The DC calculated by the 1–DOF approach differ from the results given in the literature[7] by 4.1% on average. Equations (8), (10), and (11) were obtained independently by applying the fundamental laws of fluid flow to the models as discussed in the Sections–*Governing equation for pressure*

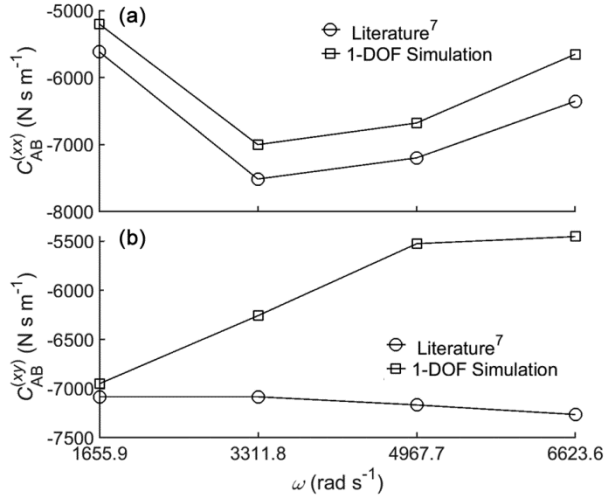

Fig. 13 — Dynamic characteristics of air–bearing: (a) Direct damping coefficients, (b) Cross–coupled damping coefficients ($C_{\mathrm{AB}}^{(xx)} < 0$ at the given range of ω; A negative damping coefficient increases the amplitude of self–excited vibrations and results in "air hammer effect" on the rotor)

distribution in air–bearing and *Governing equations for mass flow through the feed–holes of air–bearing*. Again, the average percentage difference in the DC ($K_{\mathrm{AB}}^{(xx)}$ and $K_{\mathrm{AB}}^{(xy)}$ shown in Fig. 12, and $C_{\mathrm{AB}}^{(xx)}$ and $C_{\mathrm{AB}}^{(xy)}$ shown in Fig. 13) is attributed to the minor differences in the mathematical models used in this research and the literature.[7]

The numerical solution of p–distribution in the AB dictates the numerical values of $K_{\mathrm{AB}}^{(ij)}$ and $C_{\mathrm{AB}}^{(ij)}$. The numerical solution of p–distribution is obtained by discretizing the flow field with a two–dimensional grid as shown in Fig. 5. In the present computation, the number of grid points M in the ξ–direction and N in the θ–direction are varied. For each set of (M, N), the computation of DC is carried out. As the number of grid points is increased, it is found out that, for getting a stable solution for a specific air flow rate ($\dot{m}_{\mathrm{FH}}$), it is necessary to reduce the computational time–step $\Delta\tau$. $\dot{m}_{\mathrm{FH}}$ is calculated at the grid points that correspond to the locations of FH as part of the p–distribution computation, using Newton–Raphson method.

The data in Fig. 12 shows that $K_{\mathrm{AB}}^{(xy)}$ are 5–times smaller than $K_{\mathrm{AB}}^{(xx)}$. It implies that destabilizing effects associated with the hydrodynamic lubrication mechanism in AB are not negligible. From Fig. 13, it is observed that $C_{\mathrm{AB}}^{(xx)} < 0$ at the given range of ω. This fact is the cause of SE vibrations and results in "air hammer effect" on the rotor. $C_{\mathrm{AB}}^{(xx)} > 0$ implies a force that is proportional to velocity and is directed opposite to it. $C_{\mathrm{AB}}^{(xx)} < 0$ implies a force proportional to velocity but having the same direction as the velocity. Hence, a negative damping increases the amplitude of the free–vibration instead of diminishing it, resulting in SE vibrations.

Conclusions

In this paper, a Single–Degree of Freedom (1–DOF) solution procedure for determining the dynamic characteristics of the Air–Bearing (AB) is demonstrated. Pressure (p) distribution in AB is computed by solving the Reynolds Equation (RE). This equation is solved using the Alternating–Direction Implicit (ADI) finite–difference method. The ADI method results in periodic tridiagonal and tridiagonal algebraic equations. These equations are solved using a symbolic Thomas algorithm and Thomas' algorithm, respectively. The static and dynamic analyses of AB are made. The entire analysis procedure is coded using MATLAB software. The following studies are made to test the mesh sensitivity of the numerical results obtained by the 1–DOF solution procedure: (a) spatial grid independence study and (b) temporal grid independence study. This paper demonstrates that the term in the RE that represents the mass flow rate per unit volume due to the velocity–induced flow would not be present to compute the p distribution in the Air–Ring (AR) region of Air–Ring Bearing (ARB), because the bushing does not rotate. However, in the 1-DOF solution procedure reported by previous studies, the same RE was employed for computing the p distribution in the AR and AB regions of ARB. The results on eccentricity ratio obtained from the 1–DOF approach and the literature differ by 0.34%, in an average sense. The results of attitude angle differ by 61.4%. The results of dynamic characteristics differ by 4.1%. The average percentage difference in the results is attributed to the minor differences in the mathematical models used in this research and the previous studies.

Acknowledgements

The author wishes to thank Dr. Sridhar Thyageswaran, Professor (Retd.), Department of Mechanical Engineering, Coimbatore Institute of Technology, India, for his comments to improve the contents of this manuscript.

Supplementary Matter

Supplementary data of this article is available at https://nopr.niscpr.res.in/handle/123456789/46

References

1 Muthanandam M, Effects of air–ring bearing parameters on the dynamic stability of rotor air–ring bearing system, *Iran J Sci Technol Trans Mech Eng*, **49** (2025) 1051–1068.

2 Lund J W, The stability of an elastic rotor in journal bearings with flexible, damped supports, *Trans ASME J Appl Mech*, **32** (1965) 911–920.

3 Powell J W & Tempest M C, A study of high–speed machines with rubber stabilized air bearings, *Trans ASME J Lubr Technol*, **90** (1968) 701–708.

4 Majumdar B C, Stability characteristics of gas–lubricated bearings supported on rubber 'O' rings, *Tribol Int*, **8** (1975) 127–129.

5 Belforte G, Colombo F, Raparelli T & Viktorov V, High–speed rotor with air bearings mounted on flexible supports: test bench and experimental results, *Trans ASME J Tribol*, **130** (2008) 021103.

6 Brzeski L & Kazimierski Z, High stiffness bearing, *Trans ASME J Lubr Technol*, **101** (1979) 520–525.

7 Czołczyński K, *Rotor Dynamics of Gas–Lubricated Journal Bearing Systems* (Springer–Verlag, New York) 1999.

8 Kazimierski Z &Trojnarski J, Investigations of externally–pressurized gas bearings with different feeding systems, *Trans ASME J Lubr Technol*, **102** (1980) 59–64.

9 Czołczyński K, Brzeski L & Kazimierski Z, High stiffness gas journal bearing under the step force, *Wear*, **167** (1993) 49–58.

10 Czołczyński K, How to obtain stiffness and damping coefficients of gas bearings, *Wear*, **201** (1996) 265–275.

11 Czołczyński K, Kapitaniak T & Marynowski K, Stability of rotors supported in gas bearings with bushes mounted in air rings, *Wear*, **199** (1996) 100–112.

12 Czołczyński K, Stability of the rotor supported in gas journal bearings with a chamber feeding system, *Wear*, **210** (1997) 220–236.

13 Muthanandam M, Ramamurthy S & Nadarajan S, Design of air bearing for high speed micro gas turbine, in *Proc 5th Nat Sem Exh Aerosp Rt Mech* (ISRO Satellite Centre, Bangalore) 2005, 269–277.

14 Muthanandam M, Thyageswaran S, Aswin V & Rajakumaran T, Analysis of load–carrying abilities in rotor–bearing systems, in *13th Int Conf Vib Prob* (Indian Institute of Technology, Guwahati) 2017.

15 Muthanandam M & Thyageswaran S, Determination of dynamic coefficients of air–ring bearings, *J Vib Eng Technol*, **9** (2021) 1–21.

16 Muthanandam M, *Self–Excited Vibration Analysis of a Rotor Air–Ring Bearing via a Two–Degrees of Freedom Approach*, PhD Thesis, Anna University, Chennai, 2021.

17 Muthanandam M, A comparative study of the dynamic stability of a rotor supported by an air–bearing and an air–ring bearing, *Indian J Eng Mater Sci*, **30** (2023) 629–645.

18 Gao Q, Chen W, Lu L, Huo D & Cheng K, Aerostatic bearings design and analysis with the application to precision engineering: State–of–the–art and future perspectives, *Tribol Int*, **135** (2019) 1–17.

19 Zeise P & Schweizer B, Dynamics, stability, and bifurcation analysis of rotors in air ring bearings, *J Sound Vib*, **521** (2022) 116392.

20 Zeise P & Schweizer B, Vibration and bifurcation analysis of rotor systems with air ring bearings including ring tilting, *J Sound Vib*, **571** (2024) 118079.

21 Zeise P & Schweizer B, Air ring bearings: Efficient modelling and case study for improved vibration behavior and enhanced rotor stability, *J Sound Vib*, **604** (2025) 118806.

22 Battig P & Schiffmann J, Unstable tilting motion of flexibly supported gas bearing bushings, *Mech Syst Signal Process*, **162** (2022) 107981.

23 Deb R, Hunkeler A, Wilhelm D, Jenny P & Meier B H, Numerical modeling and design decisions for aerostatic bearings with relatively large nozzle sizes in magic–angle spinning (MAS) systems, *Tribol Int*, **175** (2022) 107855.

24 Lu H, Li C, Tan Z, Hua C, Lv G, Hao J & Song G, Nonlinear thermal–vibration characteristics analysis of aerostatic spindle considering coupling effect, *Int J Mech Sci*, **294** (2025) 110260.

25 Wang B, Sun Y & Ding Q, Free fluid–structure interaction method for accurate nonlinear dynamic characteristics of the plain gas journal bearings, *J Vib Eng Technol*, **8** (2020) 149–161.

26 Chen P, Ding J, Zhuang H & Chang Y, A novel method for studying fluid–solid interaction problems of the rotor system in air bearings with manufacturing errors, *Mech Syst Signal Process*, **202** (2023) 110709.

27 An L, Wang W & Wang C, Dynamic modeling and analysis of high–speed aerostatic journal bearing–rotor system with recess, *Tribol Int*, **187** (2023) 108686.

28 Katto T & Soda N, Theoretical contributions to the study of gas–lubricated journal bearings, *Trans ASME J Basic Eng*, **84** (1962) 123–131.

29 http://repository.tamu.edu/handle/1969.1/93197 (26 August 2015).

30 Anderson J D Jr, *Modern Compressible Flow with Historical Perspective* (McGraw Hill, New York) 2004.

31 https://ntrs.nasa.gov/api/citations/19650024954/downloads/19650024954.pdf (4 July 2020).

32 Elrod H G & Glanfield G A, Computer procedures for the design of flexibly mounted, externally pressurized, gas lubricated bearings, in *Proc Gas Brg Symp* (University of Southampton), 1971.

33 Gupta S K, *Numerical Methods for Engineers* (New Age International Publishers, New Delhi), 1995.

34 Anderson J D Jr, *Computational Fluid Dynamics, the Basics with applications* (McGraw Hill Education (India) Private Limited, New Delhi) 2012.

35 Jia J, Sogabe T & Li S, A generalized symbolic Thomas algorithm for the solution of opposite–bordered tridiagonal linear systems, *J Comput Appl Math*, **290** (2015) 423–432.

36 Dimofte F, Fast methods to numerically integrate the Reynolds equation for gas fluid films, in *STLE–ASME Jt Tribol Conf* (STLE, St. Louis, Missouri) 1991.

37 Versteeg H K & Malalasekera W, *An Introduction to Computational Fluid Dynamics, the Finite Volume Method* (Pearson Education, Harlow) 2009.

38 Khonsari M M & Booser R E, *Applied Tribology, Bearing Design and Lubrication* (John Wiley and Sons, New York) 2001.